Topical Issue **Open Access**

Alexis D. Ponce, Gustavo W. Bertotto*, Alberto Zanetti, Daniele Brunelli, Tommaso Giovanardi, Eugenio Aragón, Mauro I. Bernardi, Christophe Hémond, and Maurizio Mazzucchelli

Short-scale variability of the SCLM beneath the extra-Andean back-arc (Paso de Indios, Argentina): Evidence from spinel-facies mantle xenoliths

DOI 10.1515/geo-2015-0023

Received March 31, 2014; accepted February 06, 2015

Abstract: Cenozoic basalts carrying ultramafic mantle xenoliths occur in the Matilde, León and Chenque hills in the Paso de Indios region, Argentina. The mantle xenoliths from the Chenque and León hills mainly present porphyroclastic textures, whereas the Matilde hill xenoliths have coarse-grained to porphyroclastic textures. The equilibrium temperatures are in the range of 780 to 940°C, indicating a provenance from shallow sectors of the lithospheric mantle column that were subjected to a relatively low heat flux at Cenozoic Era.

According to the modal compositions of xenoliths, the mantle beneath Matilde and León hills was affected by greater than 22% partial melting, while less depleted peridotites occur in the Chenque suite (starting from 10% partial melting). Such an observation is confirmed by the partial melting estimates based on $Cr\#_{Sp}$, which vary from 8 to 14% for the selected Chenque samples and from 14 to 18% for the Matilde ones.

The common melting trend is overlapped by small-scale cross cutting local trends that may have been generated by open-system processes, such as open-system partial melting and/or post partial-melting metasomatic migration of exotic Na-Cr-rich melts.

The two main mineralogical reaction schemes are: i) the dissolution of pyroxenes and the segregation of new olivine in olivine-rich peridotites, and ii) the replacement of primary olivine by orthopyroxene±clinopyroxene in orthopyroxene-rich peridotites. These were produced by channelled and/or pervasive melt extraction/migration. Enhanced pyroxene dissolution is attributed to channelling of silica- undersaturated melts, whereas the replacement of primary olivine by orthopyroxene±clinopyroxene points to reaction with silica-saturated melts.

Late disequilibrium reactions identified in the xenoliths comprise: the breakdown of orthopyroxene in contact with the host basalt, and (rarely) reaction coronae on orthopyroxene, clinopyroxene and spinel linked to glassy veins. Such features are apparently related to the injection of melt, likely during entrainment into the host basalts and ascent to the surface.

Keywords: mantle xenoliths; alkaline basalts; Paso de Indios; Patagonia

1 Introduction

Petrological studies of mantle xenoliths provide valuable information on the structure and composition of the litho-

Alexis D. Ponce, Mauro I. Bernardi: Instituto de Ciencias de la Tierra y Ambientales de La Pampa (CONICET- UNLPam), Av. Uruguay 151, 6300 Santa Rosa, La Pampa, Argentina
***Corresponding Author: Gustavo W. Bertotto:** Instituto de Ciencias de la Tierra y Ambientales de La Pampa (CONICET- UNLPam), Av. Uruguay 151, 6300 Santa Rosa, La Pampa, Argentina, E-mail: gwbertotto@yahoo.com.ar
Alberto Zanetti: Istituto di Geoscienze e Georisorse - CNR, U.O.S. di Pavia, Via Ferrata 1, I-27100 Pavia, Italy
Daniele Brunelli: Dipartimento di Scienze Chimiche e Geologiche, Università di Modena e Reggio Emilia, P.le S. Eufemia 19, I-41121 Modena, Italy
Daniele Brunelli: Istituto di Scienze Marine - CNR, Via Gobetti 101, I-40129 Bologna, Italy
Tommaso Giovanardi: Dipartimento di Scienze Chimiche e Geologiche, Università di Modena e Reggio Emilia, P.le S. Eufemia 19, I-41121 Modena, Italy
Tommaso Giovanardi: Instituto de Geociências, Universidade de São Paulo, Rua do Lago, 563, Cidade Universitária, 05508-900 São Paulo, Brazil
Eugenio Aragón: Centro de Investigaciones Geológicas (CONICET-UNLP), Calle 1 N° 644, 1900 La Plata, Buenos Aires, Argentina
Christophe Hémond: Domaines Océaniques, Université de Brest, CNRS, Institut Universitaire Européen de la Mer, Place Copernic, FR-29280 Plouzané, France
Maurizio Mazzucchelli: Istituto di Geoscienze e Georisorse - CNR, U.O.S. di Pavia, Via Ferrata 1, I-27100 Pavia, Italy
Maurizio Mazzucchelli: Dipartimento di Scienze Chimiche e Geologiche, Università di Modena e Reggio Emilia, P.le S. Eufemia 19, I-41121 Modena, Italy

spheric mantle [[1, 2], among others], sometimes providing the direct evidence of metasomatic processes, such as those produced by slab-derived components at convergent margins [e.g. [3, 4]]. In southern South America, south of 33° S, multiple volcanic episodes occurred during the Cenozoic Era linked to extensional movements developed in extra-Andean back-arc. These episodes are characterized by the eruption of alkali basalts [5] that in many outcrops contain mantle xenoliths. Ultramafic xenoliths are reported in different locations in Patagonia: mantle inclusions from the Comallo Region (Río Negro province) and Los Adobes (Chubut province) were firstly discussed by Gelós and Hayase [6]. Later, Bjerg *et al.* [7, 8], Barbieri *et al.* [9] and Rivalenti *et al.* [10] conducted regional studies based on spinel facies xenoliths collected in the Río Negro, Chubut and Santa Cruz provinces. Among these localities (more than 20), only two contain garnet- bearing peridotites: Pali Aike located in southern Patagonia [11–14] and Prahuaniyeu, located in northern Patagonia [8, 15–17].

In the Paso de Indios area, central region of the province of Chubut, there are several outcrops of Cenozoic basalts carrying ultramafic xenoliths. These xenoliths were first mentioned by Alric *et al.* [18], Labudía [19] and Alric [20]. Later, Rivalenti *et al.* [10] and Bjerg *et al.* [8] included microanalyses obtained in samples from the Paso de Indios area in their regional studies on the Patagonian mantle.

Rivalenti *et al.* [10] documented an extreme heterogeneity in the mantle xenoliths from this area, in which the trace-element composition of clinopyroxene showed a variability that nearly covered the entire compositional range exhibited by the mantle xenoliths from the extra-Andean Patagonian back-arc. In particular, Paso de Indios is one of the very few Patagonian localities in which clinopyroxene from spinel-facies peridotites has HREE depletion, suggesting pronounced degrees of partial melting. This fact allows the reconstruction of the mantle composition before regional reworking of the lithospheric mantle owing to the ascent of different kinds of melts triggered by the subduction process [10].

However, the available petrochemical data [e.g. [8, 10, 19]] may not be sufficient to portray a realistic picture of the lithospheric mantle.

In this paper we present detailed petrographic analysis and major-element mineral chemistry of the spinel-facies ultramafic xenoliths hosted by Paleogene basaltic rocks of the Matilde, León and Chenque hills; and comment on the P-T-X condition of the sub-continental lithospheric mantle (SCLM) beneath Paso de Indios region.

2 Geological framework

The study area is located in the extra-Andean back-arc region of Chubut province (Figure 1), in the vicinity of Paso de Indios village (Figure 2). Several alkali basaltic necks and dikes outcrop in this area along with remnants of lava flows divided in two groups of Paleocene and Eocene age [20]. Eocene magmatic activity, documented by the rocks of the Matilde, León and Chenque hills described in this work, carry ultramafic xenoliths. The basaltic rocks intrude and cover Cretaceous sediments and are partially overlain by Quaternary debris [21–23]. The basalts are related to the Paleogene bimodal volcanism of the Piedra Parada complex [24–26], a large caldera field made up of rhyolitic ignimbrites (flare up) inter-bedded with tholeiitic and alkali basalts. This extra-Andean volcanism was generated by extensional tectonics related to a transform plate margin episode that affected the southern South America active margin from the Paleocene to the Oligocene [25]. During this stage the Aluk plate detached and a slab window opened beneath the study area.

Matilde hill is located 12 km northeast of Paso de Indios locality, at 68° 55' 26.6"W, 43° 48' 41.8"S. It is the remnant of a lava flow with a semi-circular shape of about 700 m diameter containing abundant ultramafic xenoliths up to 7 cm in size. Xenoliths were obtained from sub meter-sized *in situ* lava blocks (up to 0.6 m diameter), which contained up to 5 xenoliths per block.

León volcano is located 18 km north of Paso de Indios, at 69° 0' 14.2"W, 43° 42' 8.9"S. It comprises a main hill surrounded by several smaller elevations. The outcrops are partly covered by Holocene sediments and basaltic debris. Ultramafic xenoliths are difficult to extract, being hosted in the centre of massive blocks of basalt (up to 0.8 m diameter). The maximum size of these xenoliths reaches 10 cm in diameter.

Chenque hill is a basaltic dike about 50 m long situated 26 km northeast of Paso de Indios village, adjacent to the Provincial Route 12 at 68° 56' 37.1"W, 43° 38' 36.6"S. The largest ultramafic xenoliths are up to 20 cm in diameter: they appear as loose and friable fragments scattered on the ground. Fresh xenoliths, not exceeding 5 cm in diameter, were obtained from vertical slabs of massive basalt. Chenque hill outcrops also contain a significant amount of xenoliths of lower crustal granulites, up to 25 cm in diameter, which are dominantly from the Jurassic Period [27]. This locality is different from that named Cerro de los Chenques reported in Rivalenti *et al.* [28] and located approximately 160 km to the southwest at 70° 4' 9.9"W, 44° 52' 2.9"S.

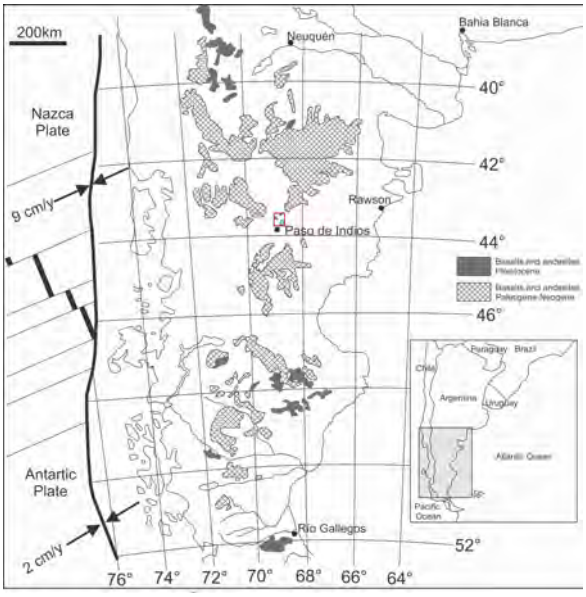

Figure 1: Location of Paso de Indios area in the context of back-arc Tertiary volcanism of Patagonia, modified after Rivalenti *et al.* [28].

3 Material and methods

We carried out the petrographic description and modal analyses of 19 spinel-facies ultramafic xenoliths from León hill, 27 from Matilde hill and 20 from Chenque hill.

The modal analysis of the xenoliths was carried out on thin section scanned images using the software Rock.Ar [29]. The number of counts per section varies between 3000 and 7000. Accuracy of the results of the software-based modal analysis was cross-checked manually on the optical microscope fitted with an integrated stage and an automatic point counter. Analyses of about 20 thin sections did not show significant difference in the estimated percentages of the mineral phases.

The major-element chemical composition of olivine, orthopyroxene, clinopyroxene and spinel was determined with a JEOL JXA-8200 electron microprobe in wavelength dispersive mode at Dipartimento di Scienze della Terra, Università di Milano, Italy, using 15 kV accelerating voltage, 15 nA beam current, 1-3 μm beam diameter, 30 s counting time on the peaks and 10 s on the background. Natural minerals (olivine for Mg; omphacite for Na; ilmenite for Ti; rodonite for Mn; K-feldspar for K; anorthite for Al and Ca; wollastonite for Si; fayalite for Fe and nicolite for Ni) and synthetic chromite were used as standards. The results were corrected for matrix effects using the conventional ZAF method provided by the JEOL suite of programs. Results are considered to be accurate within 2–6%.

4 Petrography and classification of the xenoliths

Xenoliths sampled from León hill are spinel peridotites and pyroxenites (Figure 3, Table 1). Harzburgite is the most frequent rock type (8 samples, 42%), followed by lherzolite (5 samples, 26%), dunite (3 samples, 16%), olivine-websterite (2 samples, 11%) and wehrlite (1 sample, 5%). The dominant texture is porphyroclastic (58%) and, less frequently, porphyroclastic transitional to equigranular (21%), coarse-grained to porphyroclastic (16%) and coarse-grained (5%) (Figure 4A). Modal content of olivine in peridotites ranges from 60 to 89 vol.%, while in the two olivine-websterites is slightly above 5 vol.%. Large olivines are anhedral to subhedral: they show kink bands and reach 12 mm in length. Small, unstrained grains, up to 1–2 mm, have polygonal edges with frequent triple junctions. In dunites (L16, L76, L82b) and olivine-rich (>74 vol.%) peridotites (L17, L20, L37, L69, L72) small grains of unstrained olivine are located in orthopyroxene embayments suggesting replacement (see pictures and discussion in [30]). The modal content of orthopyroxene ranges from 2 to 38 vol.% in peridotites, and approximately 87 vol.% in olivine-websterites. The orthopyroxenes are mainly anhedral and reach 12 mm in diameter (Figure 4A). Large grains commonly show a thin regular pattern of clinopyroxene exsolution lamellae and kink-bands less developed than those present in olivine. Orthopyroxene shows reaction rims when in contact with the host lava constituted by clinopyroxene + olivine + glass ± orthopyroxene ± spinel group minerals ± plagioclase, generally less than 0.6 mm thick. In orthopyroxene-rich samples (L38, L59, L68, L73, L82a), frequently small orthopyroxene shows a vermicular texture inside or between larger and strained olivine grains suggesting replacement (see [30]), locally in association with clinopyroxene and smaller and unstrained olivine. The modal content of clinopyroxene in olivine-websterites is approximately 5 vol.%, whereas it varies between 0.2 and 14 vol.% in harzburgites and lherzolites, reaching 26 vol.% in wehrlite L75. In lherzolite and harzburgite, clinopyroxene occurs as anhedral crystals up to 1.2 mm in diameter (Figure 4A), while in wehrlite L75 large clinopyroxenes enclose olivine and minor orthopyroxene defining a poikilitic texture. In dunites and olivine-rich harzburgites, clinopyroxene is scarce and interstitial, being associated with secondary olivine replacing primary orthopyroxene. Rarely, it shows a cloudy appearance due to the presence of tiny (<30 μm diameter) melt inclusions. The modal content of spinel varies from 0.6 to 3 vol.% in peridotites and from 0.7 to 1.4 vol.% in olivine-websterites.

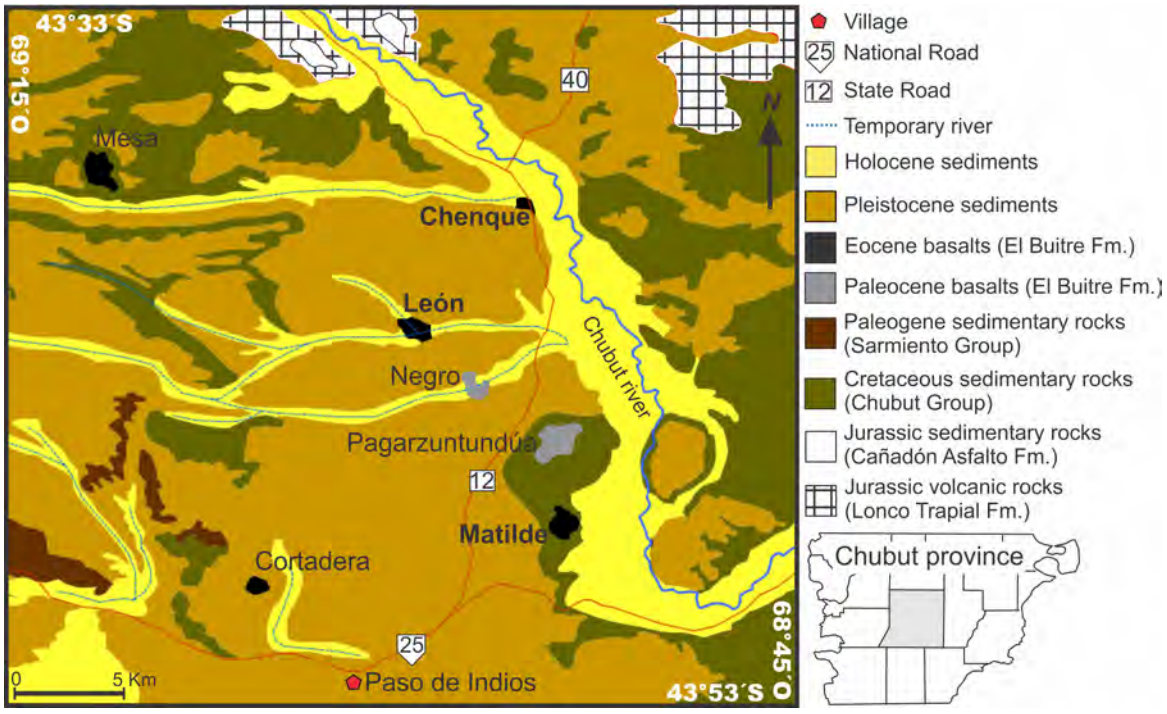

Figure 2: Geological sketch of the study area, after Alric *et al.* [21], Anselmi *et al.* [22] and Silva Nieto [23]. The studied outcrops are shown in bold style.

Spinel occurs with three different habits (e.g. in harzburgite L82a). Larger spinels occur as anhedral grains (holly leaf), reaching 2.7 mm in length. A second group is represented by subhedral and euhedral inclusions in olivine. Spinel is also present as rounded grains associated with secondary olivine and clinopyroxene replacing larger, primary orthopyroxenes. Veinlets of altered (serpentinized) glass are common in the studied samples. They form up to 6 % of the rock volume, being frequently directly linked to the host basalt.

Xenoliths from Matilde hill are represented by harzburgites (22 samples, 81%) with minor lherzolites (5 samples, 19%) (Figure 3, Table 1). The dominant textures are coarse-grained transitional to porphyroclastic (55%) and porphyroclastic (41%), with a small proportion of coarse-grained texture (4%) (Figure 4B). Several xenoliths bear veinlets of altered (serpentinized) glass that reach up to 5 vol.% and are frequently linked to the host basalt. Related to these veinlets, reaction zones up to 6 mm thick are observed in four samples.

Olivine content varies from 52 to 80 vol.%. Large olivine crystals reach 12 mm in diameter. They are anhedral to subhedral and kink-banded. Smaller olivines, up to 1–2 mm, are subhedral with frequent triple junctions and generally unstrained. Orthopyroxene content ranges from 8 to 40 vol.%, crystals have a maximum length of 9 mm and are mainly anhedral. Large orthopyroxenes show exsolution lamellae of clinopyroxene. In olivine-rich harzburgites (MA, M14, M15, M17), orthopyroxene is frequently interstitial and vermicular, replacing large strained olivines. Orthopyroxene in contact with basalt developed a reaction texture composed mainly of secondary clinopyroxene and minor glass, spinel group minerals, orthopyroxene, plagioclase and olivine. Lherzolites M23 and M66 show orthopyroxenes almost totally replaced by a fine-grained intergrowth of clinopyroxene and olivine (up to 0.3 mm in diameter): such reaction zones are linked to veinlets of altered glass directly connected with host basalt.

Clinopyroxene has a variable modal content ranging from 0.3 to 8.5 vol.%, it is anhedral and up to 3 mm in size. Spinel reaches 2.5 mm in size, is anhedral and spans from 0.2 to 6.6 vol.%. Holly-leaf shaped spinel [31] is commonly observed in porphyroclastic samples.

At Chenque hill, most of the ultramafic xenoliths can be classified as lherzolites (8 samples, 42%) and harzburgites (7 samples, 37%); a few websterites (3 samples, 16%) and only one dunite (1 sample, 5%) were also observed (Figure 3, Table 1). One sample of peridotite (Q98) with a pyroxenite band (composite xenolith) was found. Textures identified, in order of decreasing abundance are: porphyroclastic (53%), porphyroclastic to equigranular

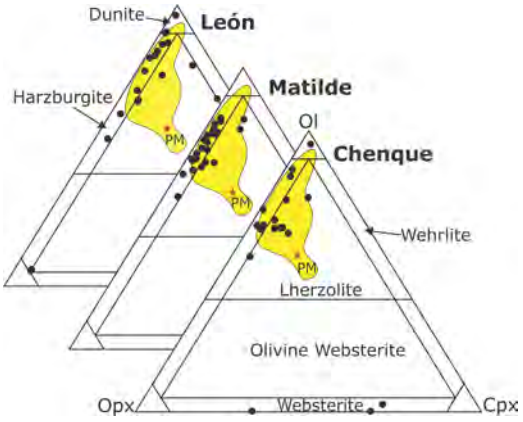

Figure 3: Modal distribution of Paso de Indios xenoliths. PM: primitive mantle from Johnson *et al.* [32]. The yellow field represents the variation of anhydrous Patagonian xenoliths from Bjerg *et al.* [8] and Rivalenti *et al.* [10].

(26%), equigranular (11%), coarse-grained to porphyroclastic (5%) and coarse-grained (5%) (Figure 4C). Olivine modal content varies between 54 to 92 vol.% in peridotites and from 0 to 3 vol.% in websterites. Large anhedral to subhedral crystals of olivine reach 10 mm, have irregular edges and show kink-bands (Figure 4D). Olivine smaller than 1.5 mm is polygonal and mainly unstrained. Unlike the León samples, evidence of small olivine grains replacing orthopyroxene was found in only one olivine-rich harzburgite (Q101, Figure 4E). The modal content of orthopyroxene varies between 1 to 37 vol.% in peridotites and from 26 to 66 vol.% in websterites. Subhedral grains of orthopyroxene, reaching 10 mm in diameter, frequently show exsolution lamellae of clinopyroxene and sometimes kink-bands. Orthopyroxene, sometimes associated with clinopyroxene (Figures 4D, F), frequently replaces strained olivine in samples with more than 22 vol.% orthopyroxene (Q58, Q59, Q65, Q96, Q103, Q104, Q105, Q107, Q109, Q-EUG). Less frequently, large crystals of orthopyroxene with exsolution lamellae and kink-bands exhibit embayments occupied by small grains of olivine ± clinopyroxene (e.g. harzburgite Q101, Figure 4E). As in the other localities, orthopyroxene shows reaction textures where it comes in contact with the host lava (Figures 5A-C). Clinopyroxene is anhedral, reaching up to 2.5 mm in diameter and its modal content ranges from 1 to 12 vol.% in peridotites and from 34 to 68 vol.% in websterites. Rarely, clinopyroxene shows reaction (spongy) rims with the development of a corona (<0.3 mm) consisting of smaller grains of clinopyroxene enriched in Mg and Ca and depleted in Al and Na in relation to clinopyroxene core. Spinel is anhedral, reaches 2 mm in size, and its modal composition range between 1 and 4 vol.% in peridotites and from 0 to 1.4 vol.% in websterites. Holly-leaf shaped spinel is commonly observed in porphyroclastic samples. Chenque xenoliths show up to 3 vol.% glass-altered veinlets, frequently linked to the host basalt (Figure 5A).

5 Major-element composition of minerals

Results of mineral microprobe analyses (5 xenoliths from Chenque, 5 from Matilde and 1 from León) are shown in Table 2. See Appendix for a detailed petrographic description of the analyzed samples.

At León hill in the only sample analyzed (harzburgite-L82a), the forsterite (Fo) content of olivine is 91.5 mol%. Orthopyroxene is enstatitic in composition $En_{91.2–91.4}$, $Fs_{7.7–7.9}$ and $Wo_{0.9–1}$ and clinopyroxene is diopside with En48.7-49.4, Fs3.5-3.7 and Wo46.9-47.7 relative contents. The spinel Mg# [= 100*Mg/(Mg+Fe) molar ratio, all Fe as Fe^{2+}] is 78.7 (L82a), while Cr# [= 100*Cr/(Cr+Al) molar ratio] is 27.8.

Olivine from Matilde has Fo content in the range of 90.8-91.4 mol%. Orthopyroxene is enstatitic in composition spanning $En_{90.4–91.3}$, $Fs_{7.8–8.6}$ and $Wo_{0.7–1.6}$ relative contents. In orthopyroxene the Al_2O_3 content shows a weak negative correlation with MgO in Matilde samples and no correlation is found in other localities (Figure 6). Clinopyroxene is diopside with $En_{48.1–49.8}$, $Fs_{2.7–3.3}$ and $Wo_{46.9–48.9}$ contents. The Mg# of spinel ranges from 67.3 (M67) to 71.0 (M79), while Cr# varies from 37.3 (M53) to 44.4 (M67 and M55) (Figure 6). Matilde xenoliths have pyroxene with the lowest Al content and spinels with the highest Cr# (Figure 6) in our sample dataset.

Olivine from Chenque hill has the widest range of variation in Fo content, from 92.0 mol% in the harzburgite Q101 to 90.2 mol% in lherzolite Q-EUG. As in León

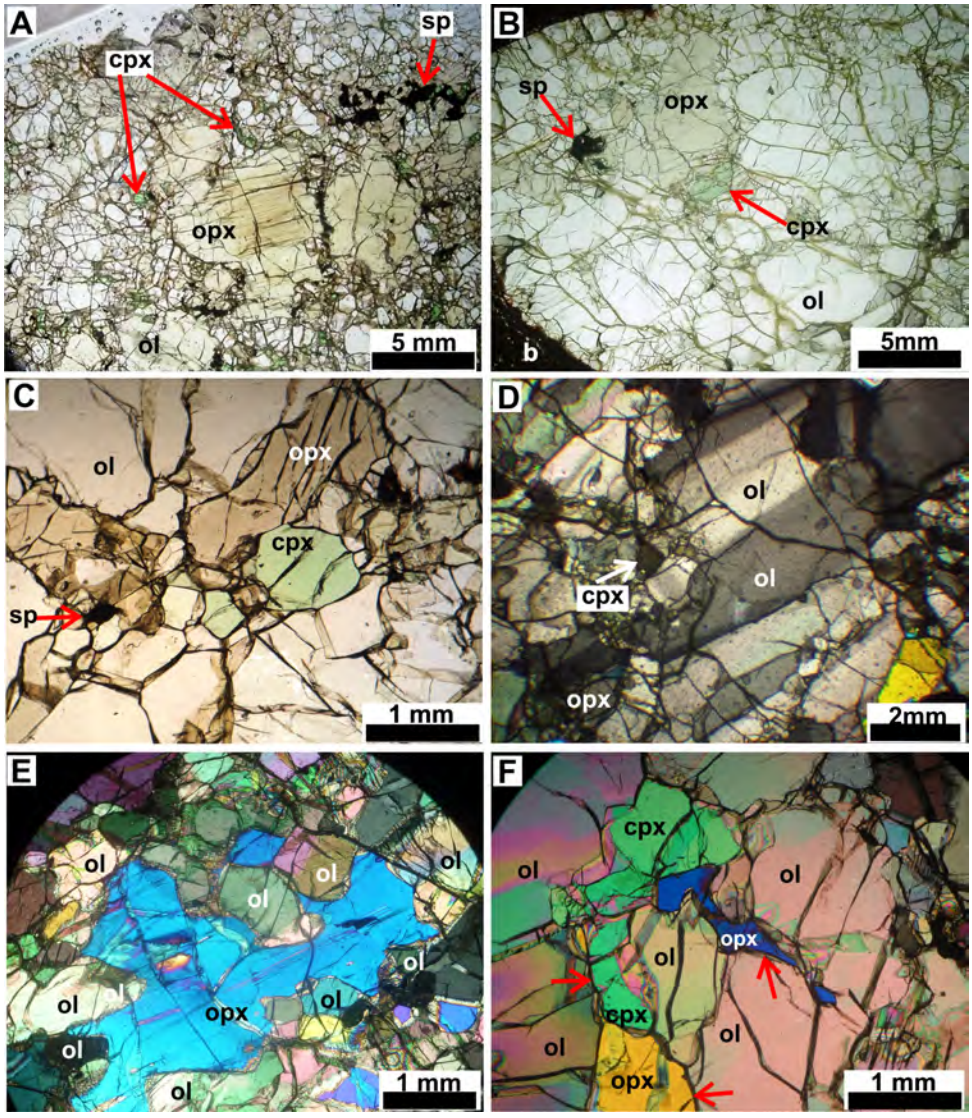

Figure 4: Microphotographs in plane-polarized (A, B, C) and cross-polarized (D, E, F) light of ultramafic xenoliths. (A) Porphyroclastic transitional to equigranular texture in harzburgite of León hill (L82a). (B) Coarse- grained transitional to porphyroclastic texture in harzburgite of Matilde hill (MH). (C) Detail of porphyroclastic to equigranular texture in lherzolite of Chenque hill (Q-EUG). (D) Crystallization of small pyroxenes and unstrained olivines around kink-banded olivine in coarse-grained to porphyroclastic harzburgite of Chenque hill (Q84). (E) Embayed orthopyroxene with crystallization of smaller olivine in harzburgite Q101. (F) Orthopyroxene and clinopyroxene (arrows) replacing strained olivine in lherzolite Q-EUG. The colours in microphotographs A-F are corresponding to sections of c.a. 120 μm thick.

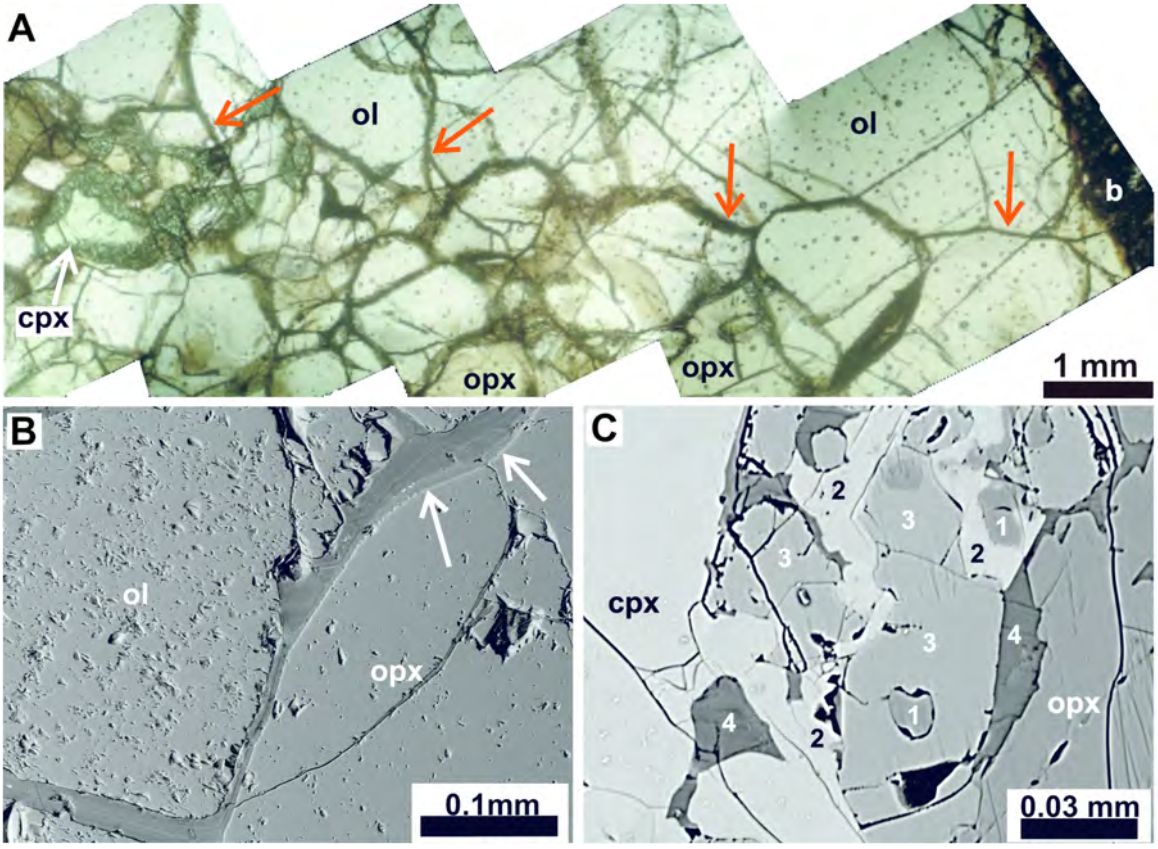

Figure 5: Microphotographs in plane-polarized (A) light of the Chenque hill (Q96) ultramafic xenolith, and backscattered SEM images (B, C). (A) Optical image (composed of four photos) of lherzolite with porphyroclastic transitional to equigranular texture of Chenque hill (Q96). Note the reaction coronae rimming clinopyroxene and a veinlets (diameter <0.1 mm) network (red arrows) which connect with hosting melt ("b"). (B) SEM image of melt vein reacting (dissolving) orthopyroxene (arrows) in harzburgite of Matilde hill (M67). (C) SEM image of the products of reaction between basalt, clinopyroxene and orthopyroxene in websterite from Chenque hill (Q77); 1, orthopyroxene; 2, clinopyroxene; 3, olivine; 4, trachytic glass. Ol, olivine; opx, orthopyroxene; cpx, clinopyroxene; sp, spinel. The colours in microphotograph A are corresponding to a section of c.a. 120 μm thick.

Table 1: Modal compositions and texture of León (L), Matilde (M) and Chenque (Q) xenoliths, based on point counting analysis. Minerals in volume%. In italics samples with microanalyses. Porph = porphyroclastic; CG = coarse-grained; Equi= equigranular.

Sample	Ol	Opx	Cpx	Sp	Veins	Total	Rock	Texture
L8	78.9	16.3	0.8	1.2	2.8	100	harzburgite	Porph.
L12	76.7	5.8	13.8	1.3	2.4	100	lherzolite	Porph.
L16	87.8	7.7	0.1	0.6	3.8	100	dunite	CG to Porph.
L17	84.3	8.6	3.2	2.1	1.9	100	harzburgite	Porph. to Equi.
L20	84.5	10.5	1.8	1.9	1.3	100	harzburgite	Porph.
L35	74.6	16.2	7.2	1.7	0.3	100	lherzolite	Porph.
L37	77.3	11.4	6.5	3	1.8	100	lherzolite	Porph.
L38	65.9	27.1	5	0.8	1.1	100	lherzolite	CG to Porph.
L59	67.9	25.5	3	1.5	2.1	100	harzburgite	Porph. to Equi.
L61	5.6	86.6	5.2	0.7	1.9	100	ol-websterite	CG
L64	5.3	86.7	5.2	1.4	1.4	100	ol-websterite	CG to Porph.
L68	60.2	34.2	2.6	2.3	0.6	100	harzburgite	Porph.
L69	74.4	19.9	1.5	3.3	0.8	100	harzburgite	Porph.
L72a	80	14.4	1.7	0.7	3.1	100	harzburgite	Porph.
L73	65.8	27.9	5.1	1.2	0.04	100	lherzolite	Porph. to Equi.
L75	64.5	4.7	25.8	1.3	3.6	100	wehrlite	Porph. to Equi.
L76	87.7	8.6	0.8	2.4	0.5	100	dunite	Porph.
L82a	*54.1*	*38.1*	*3.6*	*2.8*	*1.4*	*100*	*harzburgite*	*Porph.*
L82b	89	1.8	0.2	3.2	5.8	100	dunite	Porph.
MA	75.8	18.1	1.5	1.4	3.2	100	harzburgite	CG to Porph.
MB	75.8	19.6	3.2	0.9	0.5	100	harzburgite	CG to Porph.
ME	76.3	19.2	1.7	0.2	2.6	100	harzburgite	CG to Porph.
MH	*67.9*	*27.9*	*1.3*	*2*	*0.9*	*100*	*harzburgite*	*CG to Porph.*
MI	78.4	14.5	1.6	0.6	4.9	100	harzburgite	CG to Porph.
M2	62	31.7	3.3	1	2.1	100	harzburgite	CG
M13	72.6	21.2	1.2	2.2	2.8	100	harzburgite	CG to Porph.
M14	75	18.9	2.7	2	1.4	100	harzburgite	Porph.
M15	71.7	23.1	2.3	0.5	2.3	100	harzburgite	CG to Porph.
M17	68.2	24	3.5	0.8	3.6	100	harzburgite	Porph.
M23	78.1	8.7	8.2	1.6	3.4	100	lherzolite	Porph.
M25	70.8	22.8	0.9	3.2	2.3	100	harzburgite	CG to Porph.
M31b	63.3	28.8	4.9	1.6	1.4	100	lherzolite	Porph.
M37	63.9	29.5	1	2.3	3.2	100	harzburgite	Porph.
M41	78.2	17.5	1.2	1.8	1.3	100	harzburgite	CG to Porph.
M53	*63.9*	*24.2*	*7.7*	*2.5*	*1.8*	*100*	*lherzolite*	*Porph.*
M55	*74.3*	*20.1*	*2*	*2.1*	*1.4*	*100*	*harzburgite*	*CG to Porph.*
M57	77.2	15.1	2.3	3.1	2.2	100	harzburgite	Porph.
M66	72	11	8.5	6.6	1.9	100	lherzolite	Porph.
M67	*68.4*	*25.1*	*1.8*	*4*	*0.7*	*100*	*harzburgite*	*CG to Porph.*
M68	75.1	18.3	3.1	1.4	2.1	100	harzburgite	CG to Porph.
M71	59.8	34.7	0.9	3.8	0.8	100	harzburgite	CG to Porph.
M74	80.3	15.4	1.5	2.1	0.7	100	harzburgite	CG to Porph.
M75	67.4	29.2	2	0.6	0.8	100	harzburgite	Porph.
M76	64.8	29.4	0.3	2.3	3.1	100	harzburgite	Porph.
M77	64.8	26.7	5.2	2.3	1	100	lherzolite	Porph.
M79	*52.9*	*40.3*	*3.4*	*3.2*	*0.2*	*100*	*harzburgite*	*CG to Porph.*

Table 1: Continued.

Q53	63.5	24.1	8.8	2.2	1.4	100	lherzolite	Porph.
Q58	65.3	30.2	1.9	2.3	0.3	100	harzburgite	Porph.
Q59	53.8	37.4	5.2	3.6	0	100	lherzolite	Porph.
Q65	*62.8*	*22.9*	*9.3*	*3.9*	*1.1*	*100*	*lherzolite*	*Porph. to Equi.*
Q77	0.03	65.9	34	0	0	100	websterite	Porph. to Equi.
Q84	81.2	11.5	3.8	1.1	2	100	harzburgite	Porph.
Q91	3	26.3	68.5	1.4	0.9	100	websterite	Equi.
Q96	59.5	29.9	8.3	2.2	0.2	100	lherzolite	Porph. to Equi.
Q98	73.7	10.9	11.5	2.7	1.2	100	lherz + pyrox	Porph. + Equi.
Q101	*78.6*	*11.8*	*2.9*	*4.5*	*2.3*	*100*	*harzburgite*	*Porph.*
Q103	61.7	22.5	12	3.8	0	100	lherzolite	Porph. to Equi.
Q104	63.9	29.9	3.9	2.3	0.03	100	harzburgite	Porph.
Q105	*63.1*	*25.5*	*7.4*	*3.5*	*0.6*	*100*	*lherzolite*	*Porph.*
Q107	*73.4*	*17.4*	*5.7*	*2.6*	*0.9*	*100*	*lherzolite*	*Porph.*
Q108	82.5	10.4	2.2	2	2.9	100	harzburgite	Porph.
Q109	63.1	27.5	3.7	2.8	2.9	100	harzburgite	Porph.
Q110	0.03	31.4	67.3	1.3	0	100	websterite	Equi.
Q122	91.6	1	3	4.2	0.2	100	dunite	CG
Q132	70.5	25.8	1	2	0.7	100	harzburgite	CG to Porph.
Q-EUG	*65.5*	*23.9*	*6*	*4.2*	*0.6*	*100*	*lherzolite*	*Porph. to Equi.*

and Matilde samples, orthopyroxene from Chenque is enstatitic in composition with $En_{89.9–91.5}$, $Fs_{7.6–9.2}$ and $Wo_{0.8–1}$ relative contents. Clinopyroxene is diopside with $En_{48.1–49.1}$, $Fs_{3.0–4.2}$ and $Wo_{47.4–48.4}$ relative contents. The Mg# of spinels ranges from 70.4 (Q-EUG) to 77.9 (Q105), while Cr# varies from 20.3 (Q65) to 30.5 (Q-EUG) (Figure 5). The least depleted pyroxene and spinels from Chenque belong to lherzolite Q65.

As a whole, olivine has Fo content in the range of variation of previously published data [10]. The Na_2O and TiO_2 contents in clinopyroxene increase while CaO and MgO decrease with the increase of Al_2O_3 content (Na_2O and CaO analyses are shown in Figure 6). The content of Al, Ca and Na in the clinopyroxene of the harzburgite L82a from León hill is as high as in those from the Chenque lherzolites (Figure 6). Spinels and olivine plot within the olivine–spinel mantle array field [33]. In this diagram, some Chenque lherzolites and all the Matilde xenoliths lie very close to depletion trend estimated at 1.5 GPa. Conversely, the León sample and some other Chenques xenoliths lie apart, showing relatively large Fo contents with respect to their low Cr#Sp values (Figure 6).

The values of CaO, Na_2O and Al_2O_3 in clinopyroxene, and the Mg# and Cr# of spinels, show a range of variation comparable to previous data from Paso de Indios peridotites [8, 10], and are significantly depleted compared to the fertile mantle below the Agua Poca region (Group 1 xenoliths of [34]]), and below the Cerro de los Chenques volcano (sample CD61 of [10, 28]), which are among the very few examples of fertile spinel lherzolites with Depleted Mantle affinity found in the Argentinean extra-Andean back-arc [28, 34].

Orthopyroxene–clinopyroxene textural relationships and the positive correlation of their Mg#, Al_2O_3 (Figure 7) and TiO_2 (not shown) suggest that these two phases approach chemical equilibrium. Similarly, olivine–spinel textural relationships and the negative correlation of their Mg# suggest chemical equilibrium among these two phases in lithologies that experienced different degrees of partial melting. However, the Matilde samples on one side and the Chenque and León samples on the other side form two distinct sub-trends, in which the Mg# are positively correlated.

6 Discussion

Temperature and pressure

Estimated equilibrium temperatures of the studied xenoliths based on major-element analyses of clinopyroxene and orthopyroxene cores are shown in Table 3. Temperatures calculated with the two-pyroxene thermometer of Taylor [T_{TA98}; [35]] range from 782 (M67) to 885°C (L82a)

Table 2: (a) EMPA analyses of olivine cores.

Sample	L82a	L82a	L82a	MH	MH	M53	M53	M53	M55	M67	M67	M79	M79	M79	Q65
Mineral	1	2	3	1	2	1	2	3	1	1	2	1	2	3	1
SiO_2	41.24	41.19	41.62	41.7	41.59	41.47	41.14	41.01	41.26	40.95	40.85	40.95	41.07	41.61	40.95
TiO_2	0.04	0.03	0.04	0	0	0.02	0.01	0.06	0	0.01	0	0.03	0	0.04	0
Al_2O_3	0	0.04	0	0.01	0	0.01	0	0	0	0	0	0	0	0.01	0
Cr_2O_3	0	0.05	0.05	0.01	0	0	0.02	0	0	0	0.03	0.01	0.11	0	0.04
FeO_{tot}	8.15	8.22	8.26	8.41	8.4	8.76	8.89	8.64	8.61	8.6	8.88	8.46	8.39	8.43	9.04
MnO	0.12	0.09	0.07	0.13	0.09	0.14	0.17	0.12	0.15	0.11	0.14	0.14	0.14	0.13	0.11
NiO	0.38	0.43	0.29	0.39	0.39	0.29	0.44	0.39	0.35	0.39	0.39	0.5	0.37	0.36	0.36
MgO	50.75	50.31	50.38	50.04	50.48	50.04	50.03	50	50.32	49.86	49.94	50.33	50.22	50.03	49.72
CaO	0.07	0.04	0.04	0.03	0.02	0.01	0.04	0.03	0.02	0.02	0.03	0.05	0.07	0.04	0.08
Na_2O	0	0.02	0	0.03	0	0.02	0.02	0	0	0.01	0.01	0	0.03	0	0
K_2O	0	0	0.01	0	0	0.02	0	0	0	0	0.01	0.01	0	0	0
Total	100.75	100.41	100.77	100.74	100.97	100.78	100.76	100.25	100.71	99.95	100.29	100.47	100.39	100.65	100.3
Fo	91.62	91.51	91.51	91.26	91.38	90.93	90.77	91.04	91.1	91.07	90.79	91.24	91.29	91.23	90.64
Fa	8.26	8.39	8.42	8.61	8.53	8.93	9.05	8.83	8.75	8.81	9.06	8.61	8.56	8.63	9.25
Teph	0.13	0.1	0.08	0.13	0.09	0.14	0.18	0.13	0.16	0.12	0.15	0.15	0.15	0.14	0.11
Mg#	91.73	91.6	91.57	91.38	91.46	91.05	90.93	91.16	91.24	91.18	90.93	91.38	91.43	91.36	90.74

Table 2: (a) Continued.

Sample	Q65	Q101	Q101	Q101	Q105	Q105	Q105	Q107	Q107	Q107	Q-EUG	Q-EUG	Q-EUG
Mineral	2	1	2	3	1	2	3	1	2	3	1	2	3
SiO_2	40.96	41.42	41.53	41.46	41.11	41.45	41.21	41.3	40.89	40.62	40.65	40.71	40.97
TiO_2	0.01	0.03	0	0.03	0	0.09	0	0.02	0.02	0.02	0.02	0.07	0.05
Al_2O_3	0.01	0	0	0	0.01	0.03	0.01	0	0.01	0	0.01	0.03	0
Cr_2O_3	0.04	0.06	0.04	0	0.04	0	0.08	0.04	0	0	0	0	0.08
FeO_{tot}	8.83	7.75	7.79	8.03	8.22	8.02	8.05	8.82	8.98	9.06	9.2	9.4	9.34
MnO	0.08	0.19	0.13	0.08	0.1	0.1	0.1	0.09	0.09	0.15	0.16	0.19	0.16
NiO	0.3	0.52	0.41	0.37	0.39	0.38	0.4	0.34	0.45	0.32	0.43	0.34	0.35
MgO	49.63	50.86	50.79	50.22	50.39	50.54	50.42	49.97	49.94	49.87	48.94	49.26	49.16
CaO	0.02	0.05	0.07	0.1	0.02	0.04	0.11	0.04	0.03	0.05	0.05	0.04	0.03
Na_2O	0	0.04	0.01	0.02	0.02	0.02	0	0.02	0	0.04	0	0	0
K_2O	0.01	0.01	0	0.01	0.01	0	0	0.01	0.01	0	0	0	0.02
Total	99.89	100.92	100.76	100.31	100.31	100.66	100.39	100.64	100.42	100.13	99.46	100.04	100.16
Fo	90.84	91.94	91.95	91.69	91.52	91.72	91.68	90.9	90.75	90.61	90.3	90.15	90.21
Fa	9.07	7.86	7.91	8.23	8.38	8.17	8.21	9	9.16	9.24	9.53	9.65	9.62
Teph	0.09	0.19	0.13	0.08	0.1	0.11	0.11	0.09	0.09	0.15	0.17	0.19	0.17
Mg#	90.92	92.12	92.08	91.77	91.61	91.82	91.78	90.99	90.83	90.75	90.46	90.33	90.37

Note: Mg# = 100(Mg/(Mg+Fe2tot))

Table 2: (b) EMPA analyses of orthopyroxene cores.

Sample	L82a	L82a	L82a	MH	MH	M53	M53	M53	M55	M67	M67	M67	M79	M79	M79
Mineral	1	2	3	1	2	1	2	3	1	1	2	3	1	2	3
SiO_2	56.59	56.53	57.02	57.63	57.64	56.77	56.74	56.74	57.41	56.63	56.72	56.99	57.1	57.36	57.47
TiO_2	0.08	0.09	0.12	0	0.01	0.05	0.08	0.08	0.01	0.02	0	0.03	0.08	0	0
Al_2O_3	2.97	3.18	2.67	2.24	2.15	2.6	2.53	2.53	1.82	1.82	2.16	1.96	1.95	2.07	1.65
Cr_2O_3	0.46	0.53	0.41	0.56	0.46	0.62	0.5	0.5	0.51	0.43	0.43	0.53	0.45	0.42	0.33
FeO_{tot}	5.01	5.09	5.09	5.44	5.21	5.54	5.67	5.67	5.52	5.39	5.63	5.59	5.48	5.43	5.1
MnO	0.09	0.12	0.15	0.14	0.13	0.12	0.18	0.18	0.08	0.11	0.13	0.1	0.1	0.06	0.15
NiO	0.03	0.06	0.07	0.11	0.09	0.11	0.17	0.17	0.07	0.04	0.12	0.06	0.08	0.05	0.15
MgO	34.04	34.09	34.05	34.41	33.97	34.1	34.49	34.49	35.12	34.76	34.7	34.16	34.36	34.68	34.66
CaO	0.48	0.47	0.51	0.42	0.81	0.37	0.52	0.52	0.37	0.41	0.44	0.42	0.38	0.44	0.48
Na_2O	0.06	0.06	0.11	0.02	0.07	0.03	0	0	0.02	0.03	0.04	0.04	0.02	0.04	0.03
K_2O	0	0	0.01	0.01	0.01	0.01	0	0	0	0	0	0	0	0	0
Total	99.82	100.22	100.18	100.98	100.53	100.33	100.88	100.88	100.94	99.66	100.37	99.88	100	100.56	100.01
Wo	0.94	0.91	0.97	0.79	1.56	0.72	0.99	0.99	0.7	0.78	0.82	0.79	0.73	0.83	0.9
En	91.38	91.26	91.16	90.93	90.47	90.82	90.41	90.41	91.15	91.13	90.73	90.72	90.98	91.07	91.34
Fs	7.68	7.83	7.86	8.28	7.97	8.46	8.6	8.6	8.15	8.09	8.45	8.49	8.29	8.09	7.76
Mg#	92.37	92.28	92.27	91.85	92.08	91.65	91.56	91.56	91.9	92	91.66	91.59	91.79	91.93	92.37

Table 2: (b) Continued.

Sample	Q65	Q65	Q65	Q101	Q101	Q101	Q105	Q105	Q105	Q107	Q107	Q107	Q-EUG	Q-EUG	Q-EUG
Mineral	1	2	3	1	2	3	1	2	3	1	2	3	1	2	3
SiO_2	56.4	56.57	56.29	56.6	56.41	56.48	56.57	56.76	57.06	56.82	56.92	56.46	56.27	56.78	56.98
TiO_2	0.02	0	0.06	0	0.07	0.03	0	0.01	0	0.08	0.05	0.07	0.08	0.1	0.06
Al_2O_3	3.08	3.26	3.14	2.88	2.76	2.75	2.81	2.84	2.81	2.86	2.81	2.62	2.54	2.54	2.47
Cr_2O_3	0.37	0.35	0.39	0.46	0.4	0.44	0.41	0.46	0.46	0.51	0.43	0.4	0.4	0.37	0.44
FeO_{tot}	5.93	5.85	5.72	5.05	4.92	5.06	5.43	5.31	5.29	5.81	5.49	5.74	5.93	5.94	5.98
MnO	0.13	0.14	0.11	0.15	0.16	0.11	0.13	0.16	0.1	0.12	0.14	0.13	0.16	0.12	0.13
NiO	0.11	0.06	0.13	0.08	0.05	0.14	0.18	0.11	0.1	0.07	0.01	0.06	0.04	0.09	0.03
MgO	34.05	33.82	34.07	34.57	34.19	34.6	34.9	34.29	34.5	34.06	34.1	34.12	33.98	33.82	33.6
CaO	0.43	0.49	0.47	0.42	0.45	0.46	0.51	0.46	0.47	0.51	0.49	0.53	0.49	0.48	0.5
Na_2O	0.02	0.02	0.04	0.03	0.04	0.03	0.03	0	0.03	0.07	0.06	0.05	0.05	0.03	0.04
K_2O	0	0	0	0.01	0	0.01	0	0	0	0	0	0	0.01	0.01	0.01
Total	100.54	100.56	100.41	100.26	99.47	100.12	100.97	100.4	100.82	100.91	100.48	100.16	99.95	100.28	100.24
Wo	0.81	0.93	0.9	0.81	0.87	0.87	0.95	0.88	0.89	0.97	0.93	1	0.94	0.93	0.97
En	90.17	90.11	90.42	91.47	91.49	91.45	90.93	90.97	91.12	90.22	90.67	90.29	90.01	90.02	89.86
Fs	9.01	8.96	8.67	7.72	7.63	7.67	8.13	8.15	7.99	8.81	8.39	8.7	9.05	9.06	9.17
Mg#	91.1	91.15	91.39	92.43	92.53	92.42	91.97	92.01	92.08	91.27	91.72	91.38	91.08	91.03	90.92

Note: Mg# = 100(Mg/(Mg+Fe2tot))

Table 2: (c) EMPA analyses of clinopyroxene cores.

Sample	L82a	L82a	L82a	L82a	MH	MH	M53	M53	M53	M55	M67	M67	M79	M79	Q65
Mineral	1	2	3	4	1	2	1	2	3	1	1	2	1	2	1
SiO_2	53.48	53.34	53.54	53.84	54.86	54.65	54.08	54.23	54.12	54.69	53.85	54.12	54.48	55.05	53.4
TiO_2	0.28	0.24	0.2	0.35	0.03	0.06	0.19	0.25	0.25	0.01	0	0.02	0	0.07	0.11
Al_2O_3	4.44	4.48	4.49	4.42	2.17	2.74	2.58	2.86	2.71	1.93	2.51	2.04	2.33	2.05	4.66
Cr_2O_3	1.12	1.26	1.19	1.24	0.76	1.13	0.93	0.88	1	0.82	1.13	0.78	0.96	0.89	1.13
FeO_{tot}	2.01	1.99	1.99	2.07	1.72	1.7	1.72	1.74	1.75	1.79	1.53	1.72	1.66	1.95	2.23
MnO	0.02	0.04	0.09	0.05	0.06	0.05	0.11	0.12	0.05	0.04	0.07	0.08	0.07	0.03	0.05
NiO	0.04	0.04	0.09	0.08	0	0.01	0.03	0	0.08	0.02	0.03	0.02	0	0	0.04
MgO	15.78	15.47	15.6	15.87	16.88	16.54	16.67	16.45	16.73	17.06	16.5	16.73	16.72	16.82	15.58
CaO	21.15	21.11	20.83	20.98	23.2	22.39	23.21	23.26	23.23	22.93	22.61	22.6	22.83	22.07	21.53
Na_2O	1.4	1.45	1.53	1.39	0.73	1.07	0.61	0.66	0.61	0.62	1.03	0.88	0.78	0.98	1.23
K_2O	0	0	0	0	0	0	0	0	0	0	0.01	0	0.01	0	0
Total	99.72	99.42	99.56	100.29	100.4	100.34	100.12	100.46	100.53	99.9	99.28	99	99.84	99.91	99.94
Wo	47.33	47.74	47.17	46.92	48.26	47.87	48.53	48.87	48.48	47.69	48.3	47.79	48.12	46.94	47.87
En	49.13	48.68	49.15	49.38	48.86	49.2	48.49	48.09	48.58	49.35	49.04	49.23	49.04	49.77	48.19
Fs	3.55	3.58	3.68	3.71	2.88	2.93	2.98	3.05	2.93	2.97	2.66	2.98	2.84	3.29	3.95
Mg#	93.33	93.27	93.32	93.18	94.59	94.55	94.53	94.4	94.46	94.45	95.06	94.55	94.72	93.89	92.58

Table 2: (c) Continued.

Sample	Q65	Q65	Q101	Q101	Q101	Q105	Q105	Q105	Q107	Q107	Q107	Q-EUG	Q-EUG	Q-EUG
Mineral	2	3	1	2	3	1	2	3	1	2	3	1	2	3
SiO_2	53.76	53.28	53.49	53.81	54.14	54.03	54.38	54.19	53.72	54.16	54.05	53.47	53.33	54.3
TiO_2	0.14	0.15	0	0.01	0.05	0	0.04	0.06	0.2	0.24	0.22	0.35	0.41	0.33
Al_2O_3	4.67	4.83	3.37	3.17	3.12	3.9	3.69	3.51	4.04	4.36	3.97	3.5	3.64	3.46
Cr_2O_3	1.07	1.18	1.02	0.93	0.79	1.28	1.18	0.98	1.06	1.25	1.06	0.96	0.95	1.02
FeO_{tot}	2.32	2.17	1.68	1.76	1.77	1.88	1.63	1.84	1.95	1.99	2.11	2.11	2.22	2.18
MnO	0.12	0.05	0.09	0.09	0.07	0.02	0.05	0.02	0.02	0.07	0.09	0.1	0.04	0.04
NiO	0.07	0.03	0.01	0.03	0.09	0.06	0.06	0.03	0.06	0.07	0.07	0.07	0.06	0.05
MgO	15.63	15.47	16.18	16.24	16.56	15.92	16.26	16.38	15.78	15.49	15.95	15.97	15.92	16.14
CaO	21.35	21.46	22.37	22.42	22.8	22	22.13	22.09	21.52	21.47	21.6	21.94	22.12	22.05
Na_2O	1.3	1.33	0.96	0.84	0.79	1.1	1.05	0.98	1.35	1.35	1.34	0.92	0.94	1.02
K_2O	0	0	0	0	0.01	0.01	0	0.01	0	0	0	0	0	0
Total	100.43	99.96	99.18	99.3	100.21	100.2	100.48	100.09	99.7	100.45	100.44	99.39	99.62	100.6
Wo	47.45	47.99	48.35	48.25	48.22	48.21	48.04	47.68	47.81	48.11	47.47	47.82	48.05	47.68
En	48.33	48.13	48.66	48.63	48.73	48.54	49.11	49.19	48.78	48.29	48.76	48.43	48.12	48.56
Fs	4.23	3.88	2.99	3.11	3.05	3.25	2.85	3.13	3.41	3.6	3.77	3.75	3.83	3.75
Mg#	92.31	92.71	94.5	94.27	94.34	93.79	94.68	94.07	93.52	93.28	93.1	93.1	92.74	92.96

Note: Mg# = 100(Mg/(Mg+Fe2tot))

Table 2: (d) EMPA analyses of spinels cores.

Sample	L82a	L82a	MH	M53	M53	M55	M67	M67	M79	M79	Q65	Q101	Q105	Q107	Q-EUG
Mineral	1	1	1	1	2	1	1	2	1	2	1	1	1	1	1
SiO_2	0.05	0	0	0.01	0.02	0	0.07	0.01	0.01	0.05	0.02	0.01	0	0	0.04
TiO_2	0.13	0.16	0.01	0.15	0.19	0.01	0.03	0.03	0.04	0.03	0.05	0.02	0.06	0.12	0.2
Al_2O_3	46.1	46.23	34.54	36.33	37.61	32.01	32.01	32.03	34.85	33.83	50.74	47.48	47.69	44.18	42.06
Cr_2O_3	26.41	26.52	35.46	33.92	33.33	38.06	37.73	38.08	35.5	36.42	19.21	23.87	24.09	27.45	27.46
FeO_{tot}	8.98	8.93	12.9	13.24	12.73	13.99	14	13.88	12.68	12.93	11.31	10.31	9.69	11.39	13.16
MnO	0.03	0.05	0.04	0.02	0.06	0.08	0.09	0.05	0.04	0.02	0.07	0.04	0.02	0.08	0.06
NiO	0.2	0.24	0.16	0.18	0.09	0.12	0.16	0.13	0.16	0.17	0.26	0.24	0.23	0.19	0.21
MgO	18.58	18.61	17.41	16.86	16.85	16.67	16.16	16.3	17.45	16.97	19.17	18.92	19.17	17.55	17.55
CaO	0	0.01	0	0.02	0.01	0	0.02	0.01	0.01	0	0.01	0	0	0	0.02
Total	100.48	100.75	100.52	100.73	100.89	100.93	100.26	100.52	100.73	100.41	100.83	100.88	100.95	100.96	100.75
Cr#	27.76	27.79	40.78	38.51	37.28	44.4	44.16	44.4	40.61	41.94	20.25	25.22	25.31	29.42	30.46
Mg#	78.67	78.8	70.63	69.42	70.23	67.99	67.3	67.67	71.03	70.05	75.14	76.59	77.91	73.31	70.39

Note: Mg# = 100(Mg/(Mg+Fe2tot)); Cr# = 100(Cr/(Cr+Al))

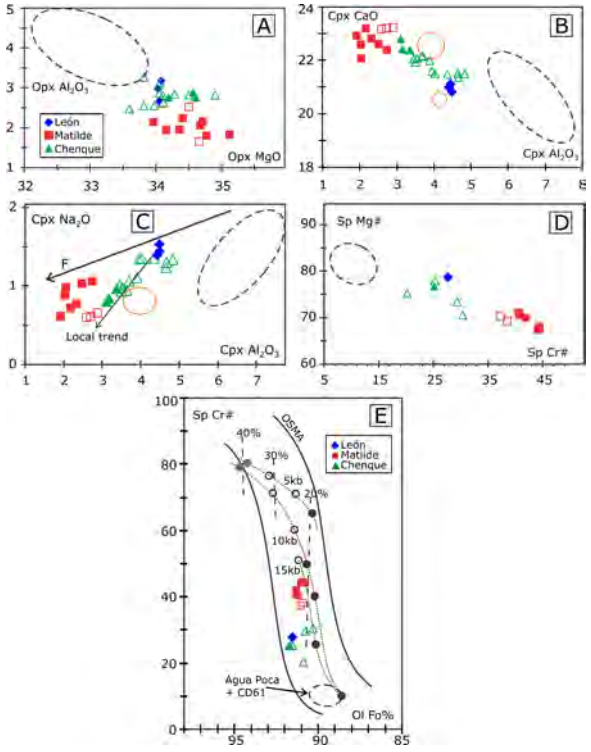

Figure 6: Major element (wt.%) variation trends in orthopyroxene (A), clinopyroxene (B–C), spinel (D) and spinel-olivine (E). Filled symbols = harzburgite; empty symbols = lherzolite. The compositional fields (orange continuous line) of clinopyroxenes from Paso de Indios after [8] are shown in B and C. All graphs show fields of variation (dashed line) of fertile mantle xenoliths from Agua Poca (37° S) (Group 1 xenoliths [34]) and Cerro de Los Chenques (sample CD61 [10, 28]) for comparison. In E, residual trends (dots lines), degree of melting and the olivine-spinel mantle array (OSMA) from Arai [33] are shown (lherzolite: full circles; harzburgite: open circles; dunite: grey circles).

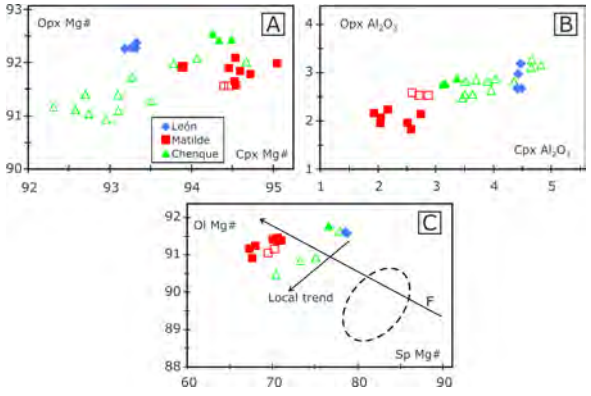

Figure 7: Correlations of Mg# and Al_2O_3 (wt.%) between orthopyroxene (A) and clinopyroxene (B); Mg# co-variation between olivine and spinel (C). Filled symbols = harzburgite; empty symbols = lherzolite. Locality symbols as in Figure 5.

(at 1.5 GPa). The temperature estimates provided by the Ca-in-Opx thermometer of Brey and Köhler [36] (T Ca-in-Opx) define a more restricted range, towards higher temperatures (861–892°C). Such a mismatch is expected according to the positive bias documented by Nimis and Grütter [37] for the Ca-in-Opx thermometer at temperatures lower than 1000°C (up to +90°C, on average, at T_{TA98} = 700°C).

Compared with the previous temperature estimates obtained using the popular two-pyroxene geothermometer (T_{BKN}; [36]) for spinel peridotites from Patagonia [8, 10, 16, 36], the T_{TA98} of the Paso de Indios samples of this study are variably lower. Temperatures (T_{BKN}) lower than 800°C were obtained only for Tres Lagos mantle peridotites [38] (T down to 728°C), even if the Tres Lagos peridotites show a maximum T up to 1040°C.

Bjerg *et al.* [8] indicated a T_{BKN} of 1030°C for one spinel harzburgite from Paso de Indios (CH-16A), whereas Rivalenti *et al.* [10] estimated T_{BKN} interval from 839 to 1197°C for 8 peridotite xenoliths from this area. Nimis and Grütter [37] demonstrated that the T_{BKN} is accurate for clinopyroxene with Na contents of ~0.05 atoms per 6-oxygen formula (apfu), but these temperature estimations show a systematic positive bias with increasing NaCpx (~150°C at NaCpx = 0.25 apfu).

Nevertheless, the T_{BKN} calculated for the Paso de Indios xenoliths are significantly lower than most of those so far reported in literature for Patagonian localities, being in the range from 797 (M67) to 942°C (L82a) (at 1.5 GPa).

A similar temperature range (T from 779 to 937°C) is also obtained using the thermometer of Ballhaus *et al.* [39] based on the Fe–Mg exchange between olivine and spinel. However the temperature gradients are different among the different xenolith suites depending on the geothermometer considered. In fact, according to pyroxene thermometers [35] the lower temperature estimates are those of Matilde xenoliths (782 to 851°C), while the higher temperatures are from Chenque and León xenoliths (834 to 885°C). Considering the Ol-Sp thermometer [39], lower temperatures are derived from the Chenque and León xenoliths (779 to 879°C), whereas the higher temperatures are those of the Matilde xenoliths (821 to 937°C).

It is concluded that the temperature range of the studied xenoliths is strongly defined, since all the geothermometers used point to the same, relatively low, T interval (780 to 940°C). The latter suggests that the studied samples come from distinctly cold, presumably shallow, lithospheric mantle sectors.

This assessment is also supported by the pressures calculated with the empirical geobarometer of Mercier [40], which vary between 1.4 and 1.8 GPa (Table 3), suggesting that the studied xenoliths belonged to a restricted mantle

Table 3: Temperature (°C) and pressure (GPa) estimations. References: T_{A98} = two-pyroxene thermometer [35]; Ca-Opx = Ca in orthopyroxene thermometer [36]; BKN = two-pyroxene thermometer [36]; Ol-Sp = olivine-spinel thermometer [39]; PMc = clinopyroxene barometer [40].

Sample	TA98	Ca-Opx	BKN	Ol-Sp	PMc
L82a	885	892	942	879	1.6
MH	812	869	830	937	1.7
M53	813	861	821	821	1.4
M55	838	859	847	912	1.8
M67	782	862	797	866	1.6
M79	851	861	887	901	1.6
Q65	882	879	923	867	1.5
Q101	834	873	852	779	1.6
Q105	877	885	907	842	1.5
Q107	865	889	922	783	1.6
Q-EUG	871	892	905	836	1.6

section spanning approximately from 47 to 60 km depth. Such pressure estimates show a broad positive correlation with the temperatures estimated according to olivine–spinel equilibrium, whereas clear correlation is not shown with respect to temperatures calculated on the basis of the pyroxene solvus.

Estimates of partial melting

The abundance (68%) of harzburgites and lherzolites with less than 6 vol. % of clinopyroxene provides evidence that the mantle column beneath the Paso de Indios is significantly depleted with respect to the modal composition of the Primitive Mantle proposed by Johnson *et al.* [32] (Figure 3). This tendency appears in the majority of Patagonian occurrences of mantle xenoliths [8, 10, 28, 41, 42]. The possible relationship of the overall depleted character with episodes of partial melting can be inferred from the relative variation of orthopyroxene (Opx) versus clinopyroxene (Cpx) in the analyzed samples as shown in the Cpx/Opx vs. Cpx plot. The peridotitic samples from the three locations approximate the depletion model trend of non-modal partial melting of a Primitive Mantle portion (Figure 8), with some outliers (M23, M66, Q98). From this plot, we infer that the most depleted samples are those of León and Matilde with modal content of pyroxene corresponding to more than 16% (most of them ≥22%) of basalt removal. The Chenque samples have a depletion level starting from 10% partial melting, even though the 50% of them shows a modal composition of pyroxene still consistent with ≥22% partial melting.

The degree of melting (F) has been also estimated on the basis of the Cr# of the spinels using the empirical equation of Hellebrand *et al.* [44] [F = 0.10*ln(Cr#sp) + 0.24]. The results suggest that the studied peridotites experienced between 8% and 16% melt extraction. Lower degrees of partial melting (8 to 12%) are estimated for the sample suites of the Chenque and León hills with respect to the Matilde hill suite (14 to 16%). The same relative variation was obtained with the alternative equation developed by Batanova *et al.* [45] [F = 9.71*ln(Cr# sp) + 25.8]. In fact, the lower partial melting estimates are provided by the Chenque and León spinels (10 to 14% of melt extraction), whereas the most depleted samples are those of Matilde with 16 to 18%.

Both equations were also applied to the compositions of the Paso de Indios spinel previously published [10]. These samples indicate a melt extraction from 9 to more than 20% and from 11 up to 24% with the equations of Hellebrand *et al.* [44] and Batanova *et al.* [45] respectively.

As expected, the modal clinopyroxene content shows a negative correlation with degree of melting (F) estimated on the basis of spinel composition, with three outliers (one for each locality, Figure 9A) and a positive correlation with the Al content of clinopyroxene.

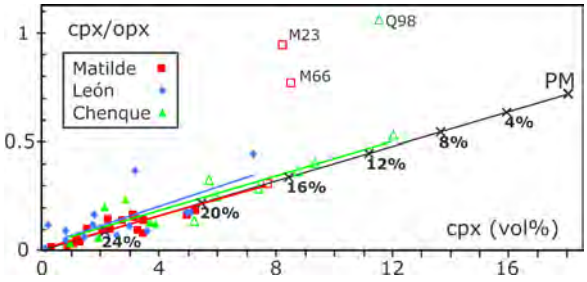

Figure 8: Cpx/Opx vs. Cpx modal relationships in peridotites from León, Matilde and Chenque hills. The regression lines for each suite are shown. Samples M23 and M66 were not included in the regression line of the Matilde samples, because of the profuse reaction of orthopyroxene with generation of clinopyroxene linked to altered-glass veins. Sample Q98 has been excluded by regression, because it is a peridotite with a band of pyroxenite (composite xenolith). The black line represents the model trend for non modal partial melting of a Primitive Mantle parcel [32] according to Rivalenti *et al.* [43]. Cross-marked intervals represent increments of 4% melting. Filled symbols = harzburgite; empty symbols = lherzolite. Locality symbols as in Figure 5.

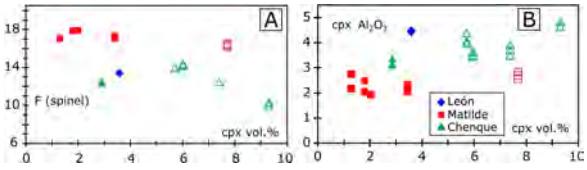

Figure 9: Correlations between the modal clinopyroxene content (vol.%) vs. (A) the degree of partial melting (F) estimated on the basis of spinel composition [45] and (B) cpx Al_2O_3 (wt.%).

Along with the opposite correlations of Na and Ca with Al content in clinopyroxene and Mg# vs. Cr# in spinel (Figure 6), these relationships are suggestive of the main compositional trend being controlled by increasing extents of partial melting of a common fertile mantle source close to the composition of the Agua Poca xenolith suite [34]. In this regard the Matilde samples are the most depleted. The mantle xenolith suite of Agua Poca has been chosen because it records fertile mineral and whole-rock composition unlike the majority of Patagonian localities.

The studied samples were recovered in a small region (<20 km apart) and belong to the same eruptive event. Along with their reduced vertical distribution they are representative of a small mantle region with respect to the scale of the partial melting processes that usually affects very large portions (hundreds of km) of the asthenospheric mantle. The observed compositional variability is therefore suggestive of short–scale variation of the apparent degree of melting that cannot be justified in terms of lateral temperature variations.

Partial melting can be locally enhanced by progressive melt channelling that induces pyroxene dissolution compositionally mimicking the partial melting trend [46]. This process is attested to by the strong orthopyroxene modal variability (Table 1, Figure 8) with several samples showing very low modal orthopyroxene and consequent locally high Cpx/Opx (Figure 8). The presence of four dunite samples can be interpreted as representative of the extreme terms of pyroxene dissolution due to channelling of silica-undersaturated melt at relatively low P [47]. Pyroxene instability is confirmed by petrographic examination that suggests a diffuse record of secondary olivine replacing orthopyroxene in olivine-rich peridotites. This process can explain differences in the inferred degree of melting, but cannot explain the compositional trends of each locality.

Compositional variations show local trends diverging from the partial melting-related trend as observed in the Na_2O vs. Al_2O_3 plot (Figure 6) and the Mg-Fe distribution between olivine and spinel (Figure 7). Peculiar trends for each locality also appear in the compositional variation of Na_2O vs. Cr# in clinopyroxene (Figure 10).

Cr# in clinopyroxene [= 100*Cr/(Cr+Al) molar ratio], increases during partial melting because of the relative compatibility of chrome with respect to aluminium. Sodium is a strongly incompatible element and is expected to decrease during partial melting. Instead, Na is observed to increase locally at increasing Cr# of the host pyroxene. Such an internal decoupling has been described in abyssal peridotites residual from the suboceanic decompressional melting [51]. The counterintuitive enrichment of the most incompatible elements during melting has been attributed

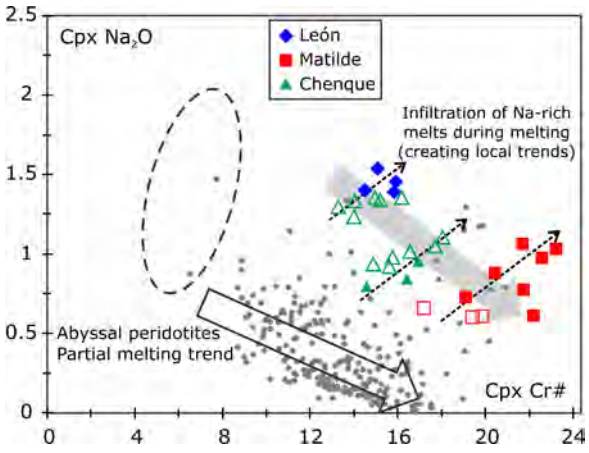

Figure 10: Clinopyroxene Na_2O vs. Cr# compositional variation in the studied samples. Grey dots show the global depletion trend defined by abyssal peridotites, which is highlighted with an empty arrow: data from the Mid Atlantic Ridge [48] and the South West Indian Ridge [49]. Dashed black line delimits the Agua Poca field after Bertotto *et al.* [34]. Local trends (arrows with dashed lines) are suggestive of open-system melting and/or metasomatism with infiltration of Na-rich melts as in Brunelli *et al.* [50]. With a grey arrow is indicated a broad negative melting-related trend of our sample suite.

to open-system melting with influx of enriched, Na-rich melts under near- batch conditions by [50]. Similar conditions can be postulated for the mantle portion during the melting event at the studied localities. As shown in Figure 10, local trends are aligned along a general trend where Cr# steadily increases while Na decreases, in conjunction with the melting trends exhibited by major oxides and the modal variations in Figures 6 and 7. The Agua Poca group 1 sample suite has a fertile end-member nature. Moreover two separate populations can be recognized among the Chenque samples, one being plotted with the León sample. The two groups are weakly recognizable in terms of major-element systematics (Figures 6 and 7). This observation may attest to the Chenque and León melt plumbing system to be partially rooted in the same mantle region. The overall melting trend runs parallel to the trend of abyssal mantle peridotites and this attests to major sodium enrichment in the analyzed suites. Whether this character pertains to the melting process itself or is due to the composition of the source and/or influxing melt, this ambiguity cannot be distinguished based on major-element data alone.

An alternative process to be considered is the possible occurrence of a metasomatic overprint due to the upward migration of exotic Na-rich mantle melt(s) unrelated to the partial melting event(s). This scenario is based on the observation that positive correlations between clinopyrox-

ene Na_2O and Cr have been documented in world-wide mantle peridotite suites belonging to craton to off-craton subcontinental realms, being basically interpreted as the result of metasomatism by alkaline melts sensu lato having large Na and Cr/Al ratios [[52] and references therein].

In this scenario, the olivine-rich lithologies were likely the preferential pathways of such melt migration, recording the highest time-integrated melt-rock ratio. Secondary olivine replacing large orthopyroxene confirms the pyroxene instability in olivine-rich peridotites.

However, the petrographic evidence of the presence of exotic melts is more effectively represented by the diffuse record of replacement of primary olivine by orthopyroxene±clinopyroxene in orthopyroxene-rich peridotites. Such a mineralogical reaction scheme points to silica- saturation in the putative migrating melt, which cannot be reconciled by closed-system partial melting processes in mantle peridotites.

This consideration is also supported by the evidence that the mineral chemistry of the sample with the largest orthopyroxene modal content, namely the harzburgite L82a from León hill, systematically shows discordant behaviour with respect to partial melting trends.

The occurrence of peridotites completely re-equilibrated by migration of LILE-enriched, HFSE-depleted melts in the Paso de Indios mantle column were already highlighted by the clinopyroxene compositions reported by Rivalenti *et al.* [10]. These authors have also provided modelling based on the trace-element composition of clinopyroxene pointing to degrees of partial melting higher than 20%.

Major-element compositional trends alone are not enough to discriminate among the proposed petrogenetic mechanisms, and trace-element modelling is hence necessary to unravel the petrogenetic processes that acted in the mantle beneath Paso de Indios. A full comprehension of the observed mineral and chemical trends would require the definition of both the composition of the infiltrating melt(s) and the melting physical conditions as the system porosity, incoming melt rate and extent of melt retention [28, 30, 50, 53, 54].

Disequilibrium reactions

In the xenoliths from the three localities, late disequilibrium reactions are locally recorded by orthopyroxene in contact with the host basalt. Less frequently, orthopyroxene in the inner part of the xenoliths shows the same disequilibrium reaction. In both cases the orthopyroxene is partially to totally replaced by an aggregate of clinopyroxene + glass + spinel group minerals + olivine ± plagioclase ± orthopyroxene. Rarely, reaction coronae surrounding clinopyroxene and spinel are present in the inner part of the xenoliths. In several samples, it is possible to identify the link between these disequilibrium reactions and the veins of altered glass that infiltrate from the host basaltic melt. The reactions presumably took place during ascent and emplacement at the surface. Several veins of altered glass located inside olivine and between olivine-clinopyroxene and olivine- orthopyroxene boundaries were analyzed by electron microprobe. In all cases the dominant components are SiO_2 (36 to 44%) MgO (29 to 36%) and FeO (5 to 8%), resembling serpentine-group mineral compositions; the analyses do not add up to 100 (analytical totals were between 76.5 and 86%) suggesting high water and volatile contents. The occurrence of serpentine in mantle xenoliths is rather frequent when the host melt is very rich in volatiles, thus determining a strong fluid activity during melt entrainment and/or emplacement to the surface, e.g. in kimberlite-borne mantle xenoliths (e.g. [55]). It is thus concluded that the Paso de Indios mantle xenoliths experienced interaction with fluids (presumably rich in volatiles) derived from the host basalt, which locally altered the primary minerals.

7 Conclusions

Peridotite xenoliths studied in this work show a mineral assemblage typical of upper mantle rocks and textures attesting to asthenospheric to lithospheric deformation and large degrees of partial melting.

The mantle portion from which the xenoliths have been extracted, experienced variable depletion by melt removal. According to the modal compositions, the mantle columns beneath the Matilde and León hills mostly recorded partial meting events greater than 22%, while less depleted peridotites occur in the Chenque suite (starting from 10% partial melting). Such an observation is confirmed by the partial melting estimates based on Cr# Sp, which vary from 8 to 14% for the selected Chenque samples and from 14 to 18% for the Matilde ones. This difference is remarkable because the localities are geographically close to each other and belong to the same volcanic event.

The common melting trend is overlapped by small-scale cross cutting local trends. Local trends can be generated by open-system processes, such as open-system partial melting in the spinel facies field and/or post partial-melting metasomatic migration of exotic Na-Cr-rich melts.

Petrographic studies confirm the occurrence of two main mineralogical reaction schemes due to channelled and/or pervasive melt extraction/migration. These are: i) pyroxene dissolution and segregation of new

olivine in olivine-rich peridotites, and ii) replacement of primary olivine by orthopyroxene±clinopyroxene in orthopyroxene-rich peridotites. Such mineralogical schemes are usually considered to be related to the migration of melts with different silica saturation.

In fact, enhanced pyroxene dissolution is attributed to channelling of silica- undersaturated melts, whereas replacement of primary olivine by orthopyroxene±clinopyroxene points to reaction with silica-saturated melts.

Further studies are required to characterise the relationships between mineralogical reactions and chemical local trends.

Late coronitic reactions involving pyroxenes and spinel are frequently linked to veins coming from the host basalt.

The studied mantle samples present the lowest temperatures so far estimated for the sub-Patagonian mantle. As a whole, geothermobarometric estimates converge in indicating that the Paso de Indios suites of mantle xenoliths derived from shallow sectors of the lithospheric mantle column, which was subjected to a relatively low heat flux with respect to other Patagonian areas during the Cenozoic.

Acknowledgement: We thank financial support of Facultad de Ciencias Exactas y Naturales (Universidad de La Pampa, Argentina - PI 235), CONICET (PIP 2011-956), and CNR-CONICET joint program (years 2013-2014). We appreciate the suggestions about fieldwork by Viviana Alric and the help during electron microprobe analyses of Andrea Risplendente. We acknowledge four anonymous reviewers that helped to improve the manuscript.

A Petrographic description of samples analyzed with microprobe

Harzburgite L82a: Porphyroclastic texture. The sample is crosscut by numerous veinlets of altered (serpentinized) glass. Large olivines are anhedral to subhedral. They show kink-bands and reach 4.5 mm in length. Frequently large olivines show embayments occupied by small orthopyroxene ± clinopyroxene ± smaller olivines. Smaller (<2 mm) mainly unstrained olivines, have polygonal edges with frequent triple junctions. Orthopyroxene is mainly anhedral, with embayments, and up to 9 mm in length. It shows kink-bands, fractures, clinopyroxene exsolution lamellae in the core, and olivine and clinopyroxene inclusions. Orthopyroxene shows disequilibrium reactions when it is placed in contact with the host basalt and/or glassy veinlets. Less common smaller grains (0.8-1.6 mm) are anhedral without exsolutions but frequently with ondulose extintion. Clinopyroxene is subhedral and up to 1.2 mm in size. Scarce clinopyroxenes have a recrystallization corona constituted by newly-formed clinopyroxene and olivine, possibly associated with glass. Spinel is present in three ways. It mainly occurs in holly leaf-shaped, up to 1.2 mm in length. Less frequently spinel is also inside glass veinlets, anhedral and up to 0.2 mm in length. Rarely, spinel is also present as skeletal grains.

Harzburgite MH: Coarse-grained to porphyroclastic texture. Olivines reach 8 mm in diameter and are kink-banded. Grains are subhedral with ragged contacts among olivines, frequently are cross-cut by numerous veinlets of altered (serpentinized) glass. Smaller olivines (<1.5 mm) are mainly subhedral. Orthopyroxene is anhedral to subhedral with curvilinear borders and 6 mm in maximum size. Orthopyroxene reacts with host basalt and glass veinlets inside xenolith. Clinopyroxene reaches 1.7 mm in size, is subhedral and shows exsolution lamellae of orthopyroxene. Spinels are subhedrals and up to 1.1 mm in diameter. Some spinels have a reaction corona in contact with orthopyroxene linked to percolating melt (glass veinlets) from host basalt. Numerous veinlets of altered (serpentinized) glass minor than 0.1 mm in diameter cross the thin section.

Lherzolite M53: Porphyroclastic texture. The thin section shows small reaction pockets and veinlets of altered (serpentinized) glass up to 0.15 mm in thickness. Olivine is subhedral, with kink-bands and ragged borders. Larger olivines reach 5 mm in length and are traversed by numerous fractures and veinlets of altered glass. Olivines, smaller than 1.5 mm are subhedral and fresh. Orthopyroxene is anhedral, fractured and reaches 8 mm in size. Orthopyroxene is also present as vermicular crystals, replacing bigger and strained olivine. In the contact with host basalt, orthopyroxene develops a thin reaction zone. Clinopyroxene is subhedral and up to 1 mm in diameter. Spinel is anhedral and reaches 0.7 mm in length. A few spinels have a reaction corona in contact with orthopyroxene as a consequence of reaction with percolating melt (glass veinlets) from host basalt.

Harzburgite M55: Coarse-grained to porphyroclastic texture. Numerous veinlets of altered (serpentinized) glass cross the sample. Porphyroclastic olivine shows kink-bands, is subhedral, reaches 10.8 mm in diameter and is crosscut by veinlets of altered glass. Larger olivines show

partial recrystallization in smaller ones. Olivines smaller than 1 mm are subhedral. Orthopyroxene is subhedral and reaches 5 mm in size. Some orthopyroxenes have fluids inclusions. Orthopyroxene develops a reaction zone, when it is in contact with basalt. Clinopyroxene is subhedral, up to 1.6 mm in diameter. Spinel reaches 1.1 mm, is anhedral and frequently is located inside olivine crystals.

Harzburgite M67: Coarse-grained to porphyroclastic texture. Olivine reaches 11.7 mm. Larger olivines show kink-bands and ragged borders. It is common the formation of euhedral, small (<1.5 mm) olivines. Orthopyroxene is anhedral, reaches 8 mm in diameter, and has exsolution lamellae of clinopyroxene. Moreover there are vermicular grains of orthopyroxene inside and between large olivine crystals. Clinopyroxenes are mainly subhedral and reach 1.4 mm. Spinel is up to 1.8 mm in size and shows vermicular texture in contact with orthopyroxene.

Harburgite M79: Coarse-grained to porphyroclastic texture. Olivine is subhedral and reaches 6.3 mm in diameter. Olivine shows kink-bands and ragged borders. Grains smaller than 1 mm are subhedral and develop triple junctions among other olivines. Orthopyroxene is mainly anhedral with maximum size of 6.7 mm. It shows irregular borders and exsolution lamellae of clinopyroxene. Vermicular orthopyroxene grains replace strained olivine. Clinopyroxene is subhedral, up to 1.4 mm in diameter. Spinel reaches 2 mm in size and has vermicular texture. Some spinels have a reaction corona linked to percolating melt (glass veinlets) from host basalt.

Lherzolite Q65: Porphyroclastic to equigranular texture. Olivine is anhedral and reaches 5 mm in size; some large crystals present ragged borders and kink-bands. Olivine grains smaller than 1 mm are subhedral, develop triple junctions and rarely are kinked. Anhedral (vermicular) crystals of orthopyroxene and clinopyroxene are located inside and between some large strained grains of olivine, suggesting replacement. Orthopyroxene is subhedral reaches 6.6 mm, showing exsolution lamellae of clinopyroxene and kink-bands. Clinopyroxene is subhedral and up to 1.2 mm in diameter. Spinel is anhedral, reaches 0.8 mm in diameter and is in contact with orthopyroxene.

Harzburgite Q101: Porphyroclastic texture. Olivine reaches 6 mm in diameter and has kink-bands. It is common to observe polygonization and recrystallization of larger olivines into smaller (<1 mm), subhedral and mainly unstrained crystals. Orthopyroxene is anhedral, reaches 5 mm in diameter and presents exsolution lamellae. Several orthopyroxenes have vermicular texture and some large grains have embayments occupied by olivine. Clinopyroxene is subhedral to anhedral and up to 1 mm in size. Spinel is subhedral, smaller than 1 mm and in contact with orthopyroxene.

Lherzolite Q105: Porphyroclastic texture. Olivine reaches 6 mm in diameter and has kink-bands. It is common polygonizationandrecrystallization of larger olivines into smaller (<1.5 mm), subhedrals and unstrained crystals. Orthopyroxene is mainly anhedral, up to 5.2 mm in length, with exsolution lamellae of clinopyroxene. Frequently small vermicular orthopyroxene grains replace strained olivine. Clinopyroxene is anhedral and up to 1.2 mm in size. Spinel is up to 1 mm in diameter and subhedral to anhedral (holly leaf-shaped).

Lherzolite Q107:Porphyroclastic texture. Numerous veinlets of serpetinized glass cross the sample. Olivine is subhedral, up to 10 mm in diameter, and with kink-bands. Unstrained olivines smaller than 1 mm are the product of recrystallization of larger ones. Orthopyroxene is anhedral, reaches 5 mm in diameter and have exsolution lamellae. Orthopyroxenes smaller than 1 mm are subhedral. Frequently vermicular orthopyroxene is replacing strained olivine. Clinopyroxene reaches 1.3 mm in diameter, is subhedral and is in contact with orthopyroxene and spinel. Spinel is subhedral and smaller than 1.1 mm.

Lherzolite Q-Eug: Porphyroclastic to equigranular texture. The investigated thin section has numerous veinlets of altered (serpentinized) glass and linked to one of them, there is a reaction zone mainly constituted by clnopyroxene ans altered glass. Larger olivines are anhedrals, have kink- bands and reach 8.5 mm in diameter. It is common to observe polygonization and recrystallization of larger olivines into smaller (<1 mm), subhedral andunstrainedcrystals. Orthopyroxene is mainly subhedral and up to 5.9 mm in size. Some orthopyroxenes show deformation lamellae. The sample has several anhedral (vermicular) orthopyroxene grains replacing olivine and apophyses of new unstrained orthopyroxene grown from the outer border of strained orthopyroxene. Clinopyroxene is anhedral to subhedral and smaller than 1.4 mm. Spinel is subhedral and up to 2.2 mm in diameter. Sometimes vermicular clinopyroxene is linked to vermicular orthopyroxene replacing large olivine grains. Spinels develop vermicular texture in contact with orthopyroxene. Spinel is also present as inclusion inside olivine.

References

[1] Comin-Chiaramonti P., Lucassen F., Girardi A., De Min A., Gomes C., Lavas and their mantle xenoliths from intracratonic Eastern Paraguay (South America Platform) and Andean domain, NW-

Argentina: a comparative review. Miner. Petrol., 2009, 98, 143–165.

[2] Karmalkar N., Duraiswami R., Chalapathi Rao N., Paul D., Mantle- derived mafic-ultramafic xenoliths and the nature of Indian sub-continental lithosphere. J. Geol. Soc. India., 2009, 73, 657–679.

[3] Zanetti A., Mazzucchelli M., Rivalenti G., Vannucci R., The Finero phlogopite-peridotite massif: an example of subduction-related metasomatism. Contrib. Mineral. Petr., 1999, 134, 107–122.

[4] Arai S., Ishimaru S., Insights into Petrological Characteristics of the Lithosphere of MantleWedge beneath Arcs through Peridotite Xenoliths: a Review. J. Petrol., 2008, 49, 665–695.

[5] Stern C.R., Frey F.A., Futa K., Zartman R.E., Peng Z., Kyser K.T., Trace- element and Sr, Nd, Pb, and O isotopic composition of Pliocene and Quaternary alkali basalts of the Patagonian Plateau lavas of southernmost South America. Contrib. Mineral. Petr., 1990, 104, 294–308.

[6] Gelós E.M., Hayase K., Estudio de las inclusiones peridotíticas en un basalto de la región de Comallo y de otras localidades de las provincias de Río Negro y Chubut. Proceedings of the 6o Congreso Geológico Argentino, Bahía Blanca (Buenos Aires), Argentina. Asociación Geológica Argentina, Buenos Aires City, 1975, 2, 69–82.

[7] Bjerg E.A., Labudía C.H., Cesaretti N., Mineralogy, texture and stress measurements of mantle xenoliths from Southern Argentina. Berichte der Deutschen Mineralogischen Gesellschaft. Beihefte zum: Eur. J. Mineral., 1991, 3, 31.

[8] Bjerg E.A., Ntaflos Th., Kurat G., Dobosi G., Labudia C.H., The upper mantle beneath Patagonia, Argentina, documented by xenoliths from alkali basalts. J. S. Am. Earth Sci., 2005, 18, 125–145.

[9] Barbieri M.A., Rivalenti G., Cingolani C., Vanucci R., Kempton P.D., 1999. Geochemical and isotope constraints on the composition of the mantle lithosphere in Patagonia (Argentina, Chile). Carlos Paz. South American Symposium on Isotope Geology, Actas, 1999, 2, 163–166.

[10] Rivalenti G., Mazzucchelli M., Laurora A., Ciuffi, S., Zanetti, A., Vannucci, R., Cingolani, C.A., The backarc mantle lithosphere in Patagonia, South America. J. S. Am. Earth Sci., 2004, 17, 121–152.

[11] Skewes, M.A., Stern, C.R., Petrology and geochemistry of alkali basalts and ultramafic inclusions from the Pali-Aike volcanic field in southern Chile and the origin of the Patagonian plateau lavas. J. Volcanol. Geoth. Res., 1979, 6, 3–25.

[12] Douglas, B.J., Saul, S.A., Stern, C.R., Rheology of the upper mantle beneath southernmost South America inferred from peridotite xenoliths. J. Geology, 1987, 95, 241–253.

[13] Stern, C.R., Saul, S., Skewes, M.A., Futa, K., Garnet peridotite xenoliths from the Pali Aike basalts of southernmost South America. In: Ross, J. (Ed.), Kimberlites and Related Rocks. Geological Society of Australia, 1989, Spec. Publ., 1989, 14(2), 735–744.

[14] Kempton, P.D., Hawkesworth, C.J., Lopez-Escobar, L., Pearson, D.G., Ware, A.J., Spinel ± garnet lherzolite xenoliths from Pali Aike: part 2. Trace element and isotopic evidence bearing on the evolution of lithospheric mantle beneath southern Patagonia. In: Gurney, J.J., Gurney, J.L., Pascoe, M.D., Richardson, S.H. (Eds.), 7th Int. Kimberlite Conf. Dawson Volume, 1999, 1, 415–428.

[15] Ntaflos, Th., Bjerg, E.A., Labudía, C.H., Thöni, M., Frisicale, C., Günther, M., Garnet-bearing xenoliths: evidence of plume activity in northern Patagonia. Abstract #3126. Proceedings of the 11th Annual Goldschmidt Conf. 2001.

[16] Bjerg, E.A., Ntaflos, Th., Thöni, M., Aliani, P., Labudia, C.H., Heterogeneous lithospheric mantle beneath Northern Patagonia: evidence from Prahuaniyeu garnet- and spinel-peridotites. J. Petrol., 2009, 50, 1267–1298.

[17] Gervasoni, F., Conceição, R.V., Bertotto, G.W., Gallas, M.R., Jalowitzki, T.L.R., Experimental petrology, geochemistry and petrography of mantle xenoliths from Prahuaniyeu Volcano, Northern Patagonia, Argentine. Goldschmidt Conf. Abstracts, Geochim. Cosmochim. Ac., 2009, 73(13), Suppl 1 A429.

[18] Alric V., Labudía C., Iglesias C., Pardo M., Xenolitos lherzolíticos en basaltos alcalinos del centro de la provincia del Chubut. Proceedings of the 12° Congreso Geológico Argentino y 2° Congreso de Exploración de Hidrocarburos, Mendoza City, Argentina. Asociación Geológica Argentina, Buenos Aires City, 1993, 4, 249–255 (in Spanish).

[19] Labudía C., Petrología y geoquímica de xenolitos lherzolíticos de las localidades de Lenzaniyeu y Paso de Indios – Comarca Nordpatagónica. Paper presented at the II Jornadas de Mineralogía, Petrografía y Metalogénesis de Rocas Ultrabásicas, Universidad Nacional de La Plata, La Plata, Argentina, 4-5 July, 1994, 3, 523–532 (in Spanish).

[20] Alric V.I., Los basaltos portadores de xenolitos aflorantes en las localidades Paso de Indios y Cerro Cóndor, departamento de Paso de Indios, provincia del Chubut. PhD thesis, Universidad Nacional de la Patagonia San Juan Bosco, Argentina, 1996 (in Spanish).

[21] Alric, V., Haller, M., Féraud, G., Betrand, H., Volcanismo Alcalino Paleógeno en los alrededores de Paso de Indios, provincia del Chubut. In: Cabaleri N., Cingolani C.A., Linares E., López de Luchi M.G., Ostera H.A., Panarello H.O. (Eds.), Proceedings of the 15° Congreso Geológico Argentino, El Calafate (Santa Cruz), Argentina. Asociación Geológica Argentina, Buenos Aires City, 2002, 2, 101–106 (in Spanish).

[22] Anselmi G., Gamba M.T., Panza J.L., Descripción geológica de la Hoja 4369-IV, Los Altares, Provincia del Chubut. Servicio Geológico Minero Argentino. Boletín N° 313, Buenos Aires, Argentina, 2004 (in Spanish).

[23] Silva Nieto, D.G., Descripción geológica de la Hoja 4369-III, Paso de Indios, Provincia del Chubut. Servicio Geológico Minero Argentino, Boletín N° 267, Buenos Aires, 2005 (in Spanish).

[24] Aragón E., Aguilera Y., Cavarozzi C., Ribot A., Basaltos Alcalinos en el Complejo Volcánico-Piroclastico del Río Chubut medio. In: Llambías E., de Barrio R., González P., Leal P., (Eds.), Proceedings of the 16° Congreso Geológico Argentino, La Plata (Buenos Aires), Argentina. Asociación Geológica Argentina, Buenos Aires City, 2005, 1, 485–486 (in Spanish).

[25] Aragón E., Brunelli D., Castro A., Rivalenti G., Varela R., Rabbia O., et al., Tectono-magmatic response to major convergence changes in the north Patagonian suprasubduction system: The Paleogene subduction- transcurrent plate margin transition. Tectonophysics, 2011, 509, 218–237.

[26] Aragón E, Pinotti L.P., D'Eramo F.J., Castro A., Rabbia O., Coniglio J.E., et al., The Farallón-Aluk ridge collisison with South America: Implications for the geochemical changes of slab window magmas from fore- to back- arc. Geoscience Frontiers, 2013, 4, 377–388.

[27] Castro A., Aragón E., Díaz-Alvarado J., Blanco I., García-Casco A., Vogt K., Liu D., Age and composition of granulite xenoliths from Paso de Indios, Chubut province, Argentina. J. S. Am. Earth Sci., 2011, 32, 567–574.
[28] Rivalenti G., Mazzucchelli M., Zanetti A., Vannucci R., Bollinger C., Hémond C., Bertotto G.W., Xenoliths from Cerro de los Chenques (Patagonia): An example of slab-related metasomatism in the backarc lithospheric mantle. Lithos, 2007, 99, 45–67.
[29] Larrea M., Martig S., Castro S.M., Aliani P., Bjerg E.A., Rock.AR – A Point Counting Application for Petrographic Thin Sections. Paper presented at the 26th Spring Conference on Computer Graphics, Budmerice, Slovakia, 13-15 May, 2010.
[30] Piccardo G.B., Zanetti A., Müntener O., Melt/peridotite interaction in the Southern Lanzo peridotite: Field, textural and geochemical evidence. Lithos, 2007, 94, 181–209.
[31] Mercier J-C.C., Nicolas A., Textures and fabrics of upper mantle peridotites as illustrated by basalts xenoliths. J. Petrol., 1975, 16, 454–487.
[32] Johnson K., Dick H., Shimizu N., Melting in oceanic upper mantle: an ion microprobe study of diopsides in abyssal peridotites. J. Geophys. Res., 1990, 95, 2661–2678.
[33] Arai S., Characterization of spinel peridotites by olivine-spinel compositional relationships: Review and interpretation, Chem. Geol., 1994, 113, 191–204.
[34] Bertotto G.W., Mazzucchelli M., Zanetti A., Vannucci R., Petrology and geochemistry of the back-arc lithospheric mantle beneath eastern Payunia (La Pampa, Argentina): Evidence from Agua Poca peridotite xenoliths, Geochem. J., 2013, 47, 219–234.
[35] Taylor W.R., An experimental test of some geothermometer and geobarometer formulations for upper mantle peridotites with application to the thermobarometry of fertile lherzolite and garnet websterite. Neues Jb. Miner. Abh., 1998, 172, 381–408.
[36] Brey G.P., Köhler T., Geothermobarometry in four-phase lherzolites II. New thermobarometers, and practical assessment of existing thermobarometers. J. Petrol., 1990, 31, 1353–1378.
[37] Nimis P., Grütter H., Internally consistent geothermometers for garnet peridotites and pyroxenites. Contrib. Mineral. Petr., 2010, 159, 411–427.
[38] Ntaflos Th., Bjerg E.A., Labudía C.H., Kurat G., Depleted lithosphere from the mantle wedge beneath Tres Lagos, southern Patagonia, Argentina. Lithos, 2007, 94, 46–65.
[39] Ballhaus C., Berry R.F., Green D.H., Experimental calibration of the olivine-orthopyroxene-spinel oxygen barometer - implications for oxygen fugacity in the Earth's upper mantle. Contrib. Mineral. Petr. 1991, 107, 27–40.
[40] Mercier J.-C.C., Single-pyroxene thermobarometry. Tectonophysics, 1980, 70, 1–37.
[41] Laurora A., Mazzucchelli M., Rivalenti G., Vannucci R., Zanetti A., Barbieri M.A., Cingolani C.A., Metasomatism and melting in carbonated peridotite xenoliths from the mantle wedge: the Gobernador Gregores case (southern Patagonia). J. Petrol., 2001, 42, 69–87.
[42] Rivalenti G., Zanetti A., Mazzucchelli M., Vannucci R., Cingolani C.A., Equivocal carbonatite markers in the mantle xenoliths of the Patagonia backarc: the Gobernador Gregores case (Santa Cruz Province, Argentina). Contrib. Mineral. Petr., 2004, 147, 647–670.
[43] Rivalenti G. et al., Composition and processes of the mantle lithosphere in northeastern Brazil and Fernando de Noronha: evidence from mantle xenoliths. Contrib. Mineral. Petr., 2000, 138, 308–325.
[44] Hellebrand E., Snow J.E., Dick H.J.B., Hofmann A.W., Coupled major and trace elements as indicators of the extent of melting in mid-ocean- ridge peridotites. Nature, 2001, 410, 677–681.
[45] Batanova V.G., Suhr G., Sobolev A.V., Origin of geochemical heterogeneity in the mantle peridotites from the Bay of Islands Ophiolite, Newfoundland, Canada; ion probe study of clinopyroxenes. Geochim. Cosmochim. Ac, 1998, 62, 853–866.
[46] Kelemen P.B., Reaction between ultramafic rock and fractionating basaltic magma I. Phase relations, the origin of calc-alkaline magma series, and the formation of discordant dunite. J. Petrol., 1990, 31, 51–98.
[47] Mazzucchelli M., Rivalenti G., Brunelli D., Zanetti A., Boari E., Formation of Highly Refractory Dunite by Focused Percolation of Pyroxenite-Derived Melt in the Balmuccia Peridotite Massif (Italy). J. Petrol., 2009, 50, 1205–1233.
[48] Brunelli D., Seyler M., Cipriani A., Ottolini L., Bonatti E., Discontinuous melt extraction and weak refertilization of mantle peridotites at the vema lithospheric section (Mid-Atlantic Ridge). J. Petrol., 2006, 47, 745–771.
[49] Seyler M., Cannat M., Mével C., Evidence for major-element heterogeneity in the mantle source of abyssal peridotites from the Southwest Indian Ridge (52° to 68°E), Geochem. Geophy. Geosy., 2003, 4(2), 9101, doi:10.1029/2002GC000305.
[50] Brunelli D., Paganelli D., Seyler M., Percolation of enriched melts during incremental open-system melting in the spinel field: A REE approach to abyssal peridotites from the Southwest Indian Ridge. Geochim. Cosmochim. Ac., 2014, 127, 190–203.
[51] Seyler M., Brunelli D., Toplis M.J., Mével C., Multiscale chemical heterogeneities beneath the eastern Southwest Indian Ridge (52°E-68°E): Trace element compositions of along-axis dredged peridotites, Geochem. Geophy. Geosy., 2011, 12, Q0AC15, doi:10.1029/2011GC003585.
[52] Nimis P., Zanetti A., Dencker I., Sobolev N.V., Major and trace element composition of chromian diopsides from the Zagadochnaya kimberlite (Yakutia, Russia): Metasomatic processes, thermobarometry and diamond potential. Lithos, 2009, 112, 397–412.
[53] Ionov D.A., Bodinier J.-L., Mukasa S.B., Zanetti A., Mechanisms and sources of mantle metasomatism: Major and trace element compositions of peridotite xenoliths from spitsbergen in the context of numerical modelling. J. Petrol., 2002, 43, 2219–2259.
[54] Raffone N., Chazot G., Pin C., Vannucci R., Zanetti A., Metasomatism in the Lithospheric Mantle beneath Middle Atlas (Morocco) and the Origin of Fe- and Mg-rich Wehrlites. J. Petrol., 50, 197–249.
[55] Kopylova M.G., Caro G., Mantle xenoliths from the southeastern slave craton: evidence for chemical zonation in a thick, cold lithosphere. J. Petrol., 2004, 45, 1045–1067.